Ember transport for bushfire simulation

Final report – Integrating a parametric ember transport scheme into the Spark bushfire simulator

Jeffrey D. Kepert[1]

1. Bureau of Meteorology

Version	Release history	Date
1.0	Initial release of document	02/02/2023

Australian Government

We acknowledge the traditional custodians across all the lands on which we live and work, and we pay our respects to Elders both past, present and emerging. We recognise that these lands and waters have always been places of teaching, research and learning.

Table of contents

Acknowledgements

1 Introduction

A parameterisation is a simplified model of a complex process, intended to be used as a component of more complex models that are unable, usually for reasons of computational cost or capacity, to resolve that process more completely. The term is widely used in atmospheric simulation, where the complex and fine-scale processes in, say, cumulus clouds or the boundary layer, are typically represented by parameterisations. If they were not, predicting the evolution of a single cumulus cloud would be capable of consuming all the computer resources available for preparing tomorrow's weather forecast. They thus represent a pragmatic solution to the problem of adequately modelling the evolution of a process that covers a very wide range of scales in time and space.

As simplified models, parameterisation development requires a careful balance between simplicity and fidelity. These two factors are more-or-less synonymous with reduced computational cost and accuracy, respectively. Parameterisation development requires that these conflicting aims be, so far as is possible, reconciled.

Firebrand transport in bushfire plumes is an example of a process that has a significant impact on the outcome of a prediction but cannot be fully resolved on present computational hardware in a sufficiently timely manner. For example, the explicit firebrand transport simulations reported by Thurston et al. (2017) consumed days of time on a supercomputer, and that was after some simplifying assumptions were made.

Firebrand transport, and the generation of spotfires, is important because it can increase the rate of bushfire spread, can cause bushfires to break containment lines, makes fires less predictable, and is often implicated in structure loss. The prediction of long-range ember transport is a particular problem for which there has been a lack of understanding and decision support tools.

Building on the work of Thurston et al. (2017) and similar results of Thomas et al. (2019), Kepert et al. (2022a,b) developed a simplified model of firebrand transport in a bushfire plume that agreed reasonably well with those explicit calculations. That model was designed to be useable as a stand-alone predictive tool, and as part of a fire-spread simulator. That parameterisation was incorporated into an earlier version of the Spark fire simulator, as described in Kepert et al. (2022a), and tested on one fire. That version of Spark was not particularly suitable for this purpose, however, with little of the necessary internal model data being readily available. However, the work yielded very encouraging results.

The aim of this project was to implement the firebrand transport parameterisation into an up-to-date version of Spark, specifically version 2. This later version is far more suitable for such tasks because the full state of the fire model is accessible to the developer, along with the ancillary data such as topography, fuels, and surface meteorology. The technical details of the implementation were described in the interim project report (Kepert 2022c). The algorithmic details are described in this report.

As already noted, the challenge with developing simplified models, such as this one, is achieving an appropriate balance between simplicity and fidelity. Almost inevitably, use of the parameterisation will reveal circumstances in which minor adjustment of the choices will improve performance. Systematic, continuous verification is crucial, both as an impetus to gradual refinement, and to enable users to interpret predictions from the model with an appropriate balance between confidence and caution. If one may make a comparison with parameterisations in numerical weather prediction systems, it is both hoped and expected that this initial version of the parameterisation will evolve and improve over time, as experience and scientific knowledge accumulate.

To begin this process of validation, the bulk of this report describes the performance of Spark with the firebrand transport parameterisation on three notable fires.

This report is organised as follows. Section 2 gives a brief overview of the formulation of the firebrand transport parameterisation, and section 3 describes some aspects of its implementation into Spark. Section 4 presents case studies of three significant fires; the Kilmore East Fire on Black Saturday, 7 February 2009; the Reedy Swamp fire of 18 March 2018; and the Timbarra fire of 25 January 2019. Section 5 presents an overall discussion of results, and section 6 highlights some outstanding issue.

End-user statement

John Bally, Fire Prediction Business Manager, AFAC

Forecasting the spread of fire is a powerful tool and as a result, bushfire simulators have become deeply integrated into the work of fire and land management agencies. There is strong recognition in the land and fire management sector of the need for a next-generation fire simulation capability. A core component of the next-generation bushfire simulator will be an ember transport and spotting sub-model that can easily be integrated into a practical simulation system. It should be able to be configured to work effectively in a full range of fuel types and a wide range of meteorological conditions and fire intensities.

The ember transport model developed in a previous project has a sound theoretical basis and requires as input, fields that will be available in simulators currently being developed. The parameterised version of the ember transport scheme captures the important features of the model and implements those in a way that can be easily integrated and most importantly, can run very efficiently in practical operational systems.

This work and the included case studies demonstrate that good simulation of bushfires needs a good simulation framework, good fire spread and ancillary models and good data. In particular the fuel data used in these case studies was the best that was easily available, but for future utilisation of this work, the quality and detail of the underlying fuel data (and weather data) is key.

The work undertaken by Dr Kepert has relied on the BARRA re-analysis dataset to estimate the vertical structure of the atmosphere above the fireground which drives the transport of firebrands. BARRA is a fabulous data set for many applications including support developments such as this and the running of case studies. The BoM is to be congratulated on developing BARRA, and should be encouraged by the fire community to maintain and improve the systems, and to develop a near real-time re-analysis to support bushfire management operations.

For more agile running of firebrand transport scheme in Spark, the development team are planning to use operational ACCESS-G forecast, and eventually move to higher resolution and ensemble Numerical Weather Prediction as it becomes operationally available. The Spark project team is very grateful to the BoM for temporarily making ACCESS-G 3D weather predictions available for Spark, is keen to work with the BoM to secure ongoing public good access to 3D and ensemble weather predictions which are becoming integral bushfire management.

This work has moved forward the science applied to the prediction of fire spread through spotting, from conceptual models and nomograms to a model with a sound theoretical basis and experimentally demonstrated through coupled fire-atmosphere numerical weather prediction modelling. As Dr Kepert has pointed out, there is much more work to do but this is a great advance. This work has also demonstrated the use of the Spark simulation framework to accommodate complex new science. The integration of new science into systems which could be used in operations has been a bottleneck for progress, often more difficult, time consuming and expensive than doing the science itself. Although this integration has not been easy and is not fully complete or sufficiently validated, this "integration" has been much quicker than is normally the case.

Thanks for the successful completion of this project go chiefly to Dr Kepert, and also to the CSIRO team, especially Dr James Hilton for providing advice and support, and for the considerable work Dr Hilton has put in to more tightly integrate this ember transport scheme into the core Spark system. Funding was provided in part by the Minderoo foundation. Thanks also go to the BoM for making Dr Kepert available for this work, and to the NHRA for facilitating the arrangements.

2 Overview of the Firebrand Transport Parameterisation

The firebrand transport parameterisation is described in full by Kepert et al. (2022a,b). We include here a brief overview for completeness.

The model consists of four main components, some of which are illustrated schematically in Figure 1. The first of these is an integral model of the time-mean plume. This is based on the equations of fluid motion, averaged across disks encompassing the plume and normal to the plume axis. There are six partial differential equations: four conservation equations for mass, energy and horizontal and vertical momentum, and two equations describing the shape of the plume. This equation set has been widely used for the simulation of buoyant plumes and jets, and the well-known Briggs model of plume rise results from further simplifying assumptions to these equations (Weil 1998). In the parameterisation, they are solved numerically, with input parameters of the meteorology (wind speed and potential temperature as a function of height) and fire properties (heat output and equivalent radius of the fire). The colour shading in Figure 1 illustrates schematically the time-mean vertical motion from this component.

The second component is a representation of turbulence within the plume. Thurston et al. (2017) demonstrated that turbulence has a profound influence on firebrand transport, and could roughly double the maximum transport distance, compared to simulations in which it was omitted. The important component of turbulence, the standard deviation of updraft fluctuations, is represented by a statistical model trained on many bushfire plume simulations in a large eddy model. Turbulence also has a spatial scale, which similarly is modelled based on these large eddy simulations.

The third component is firebrand transport within the plume. At each point in the plume, the terminal fall velocity of the firebrands is compared with the probability distribution of the updraft obtained from the first two components, as illustrated by the white inset in Figure 1. That probability, divided by the turbulence length scale, defines the rate at which firebrands fall from the plume. Integrating that rate along the plume gives the density of falling embers immediately below the plume.

The final component is the below-plume flight of the embers, which fall on a slant trajectory whose slope is the ratio of their fall velocity to the horizontal wind speed and is illustrated by the blue dashed lines in Figure 1.
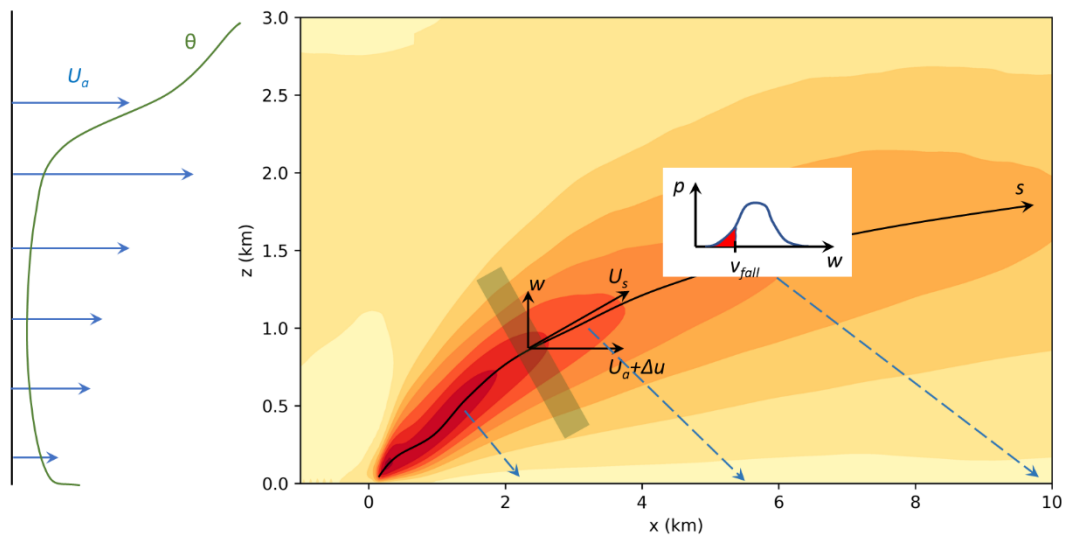
FIGURE 1: SCHEMATIC DIAGRAM OF THE EMBER TRANSPORT MODEL. THE SHADED BACKGROUND INDICATES THE VERTICAL VELOCITY, THE BLUE ARROWS TO THE LEFT THE ENVIRONMENTAL WIND U_a AND THE GREEN CURVE THE ENVIRONMENTAL POTENTIAL TEMPERATURE θ. PLUME COORDINATES ARE MEASURED BY THE CURVILINEAR AXIS s, ALONG THE PLUME AXIS. THE PLUME EQUATIONS ARE AVERAGED OVER A DISC OF RADIUS r, NORMAL TO THE PLUME AXIS, INDICATED BY THE GREEN RECTANGLE. THE VERTICAL VELOCITY HAS A PROBABILITY DISTRIBUTION DUE TO TURBULENCE, INDICATED BY THE BLUE CURVE IN THE INSET. THE PROBABILITY THAT AN EMBER FALLS FROM THE PLUME IS FOUND BY COMPARING THE EMBER TERMINAL VELOCITY v_{FALL} WITH THIS DISTRIBUTION, INDICATED BY THE RED SHADING IN THE INSET. EMBERS THAT FALL FOLLOW SLANT TRAJECTORIES, INDICATED BY THE BLUE DASHED ARROWS. FROM KEPERT ET AL. (2022B)

3 Implementation in Spark

We here describe how the ember transport parameterisation receives and interprets data from Spark to compute the plume characteristics and firebrand transport, and the new ignitions it provides back to Spark. We focus on the algorithms; the technical details of the interface between Spark and the firebrand transport parameterisation are described in the interim report (Kepert 2022c).

The key factors are the necessary fire and meteorological data for the plume calculation, and an estimate of how many new spotfire locations should be chosen by random sampling from the calculated distribution of landing positions.

The ember transport calculation does not need to be called at every Spark time step. The parameterisation employs a steady-state plume model, assumed to be in equilibrium with the source buoyancy flux and fire geometry. It is appropriate to call the plume model at an interval that reflects the time scale of plume growth, and to average the fire inputs over that interval. We have variously used 15 and 30 minutes for this interval.

Spark carries sufficient surface meteorological data for the plume calculation but does not presently hold information above the surface. This is read and stored by the initialisation step of the firebrand transport. Like the surface data, these data may be directly from observations, from numerical weather prediction, or from reanalysis.

The key fire characteristics for the plume calculation are the initial fire radius and the fire power into the plume (i.e., the initial buoyancy flux). Together with the meteorology, these determine the plume rise, shape, and updraft strength, and hence its ability to loft firebrands. The sensitivity to these parameters is discussed by Kepert et al. (2022b).

Fire power is computed from the fuel mass consumption. At each firebrand time step, the fuel mass grid is obtained from Spark. The fire power is computed from

$$H_{fire} = C \frac{\iint_A \Delta m \, dA}{\Delta t}$$

where $C = 1.86 \times 10^7 \, J \, kg^{-1}$ is the heat of combustion of cellulose, Δm is the fuel load in kg m^{-2}, and the integral is over the Spark domain. This differs from the previous implementation in that fuel within the fire is not assumed to all burn instantaneously. The heat flux into the plume is taken to be a constant fraction of the fire power to allow for losses from radiation and heating the ground (Kepert et al. 2022b),

$$H_{plume} = 0.7 H_{fire}$$

The initial radius of the plume is more difficult to determine. Physically, this represents the cross-sectional area of the plume, but using the area of the fire is not appropriate – consider, for example, a multiday fire which has burnt a large area, but has only a small active area on a given day. Some preliminary experiments with elliptical and circular fires in a large eddy model suggests that the head fire width appears to be a better proxy, although is certainly not a complete solution to the problem.

The head of the fire is defined as follows. We compute the vector displacement of each grid point within the perimeter and rotate that vector into components along and normal to the surface wind vector. We select the front 20% of points and compute the standard deviation of their crosswind displacement. The head width is defined to be 1.4 times that standard deviation; the choice of 1.4 was based on an idealised calculation with a circular fire patch. Clearly there is a degree of arbitrariness in this calculation, and we experimented with choices other than 20%. Some fires are relatively insensitive to this choice, but certainly not all. While the method appears satisfactory in most cases we have investigated, it is problematic with very long fire fronts, for example following a wind change. Better means of estimating this parameter are needed.

An appropriate number of spotfire ignitions is difficult to determine. Physically, it should depend on the rate at which firebrands are injected into the plume (the source rate), whether they burn out or otherwise self-extinguish during flight, and whether they produce a sustained ignition on landing. Important factors include the source and destination fuels, and whether fire crews are actively attacking spotfires as they ignite. At present, we make the number of ignitions proportional to the mass of forest fuel consumed. All the substantial complexity of these other factors is incorporated into the constant of proportionality, which (following some experimentation) we take to be $2 \times 10^{-7} kg^{-1}$ unless otherwise stated. While that number is certainly small, that is likely because it incorporates those other factors. The computed number of spotfires is rounded to the nearest integer.

Most simulations with spotting enabled have a period where there are from several to dozens of discrete areas of fire. It is difficult to know how to treat these. If they are sufficiently well separated, the plumes will be independent, and a separate firebrand calculation is appropriate for each. But if they are close, the plumes may merge. At present, we analyse the Spark level set variable to determine individual patches of fire. Each fire patch is treated independently for the calculation of fire power, head width, firebrand transport and number of spotfires. In order to reduce computation, fire patches with powers below 1 GW are not considered, since these small fires are generally incapable of longer-range spotting. In the future, we may experiment with allowing nearby fires to be combined for these purposes.

In the previous version, the direction of spotting was taken to be the surface wind direction. An option has been added to instead use the mean wind direction to the plume rise height.

Compared to the implementation into the previous version of Spark, these calculations have changed, mostly to be more physically representative. Fire power is now calculated from fuel consumption, rather than fire area changes. The number of spotfires is similarly calculated from the forest fuel consumption, rather than from the fire area growth.

4 Case studies

Case studies are an important component in the development of operational tools. They can illustrate the strengths and limitations of a technique and help to highlight areas where further refinement is needed. They provide examples for communication with users and stakeholders, including use in education and training. They also feed into, and eventually complement, statistical measures of forecast performance once a sufficiently large cohort of examples has accrued.

In this section, we present the results of three case studies. The specific cases were chosen based on the availability of data, and scientific and operational interest. They are the Kilmore East Fire in Victoria on Black Saturday, 7 February 2009; the Reedy Swamp fire in NSW of 18 March 2018; and the Timbarra fire in Victoria of 25 January 2019. Each were run with the same sources of fuel, topography, and meteorological data, as detailed in the following subsections. Likewise, each used the same surface spread models within Spark. Although the simulations are therefore somewhat comparable, any comparison needs to remember that the fires in reality occurred in disparate fuel, topography and meteorological conditions.

The cases were selected based on informal discussions, including at the Fire and Climate conference in Melbourne organised by the International Association of Wildland Fire in June 2022. I am grateful to Miguel Cruz for discussions and data regarding the Kilmore East fire, and to Musa Kilinc for discussions and data regarding the Timbarra fire.

Data sources

Meteorology

Meteorology for each simulation is taken from the Bureau of Meteorology Australian Region Reanalysis, BARRA. Meteorological reanalyses use state-of-the-art numerical weather prediction systems to analyze historical observations and produce a dynamically consistent, four-dimensional, gridded record of the atmosphere. BARRA covers the Australian continent and surrounds on about 12-km grid spacing, from the surface to over 40 km altitude and from 1990 to 2019 and was prepared using a version of the Bureau of Meteorology's operational assimilation and prediction system, ACCESS. Further details are in Su et al. (2019). An important advantage of BARRA is that it provides high quality upper air data needed for the plume calculation. A disadvantage relative to automatic weather station data is that the time frequency is relatively coarse, one hour instead of (up to) one minute. Thus, features such as wind changes are smoothed out in time. We choose to use just the time-series of a single column of data, rather than the full four-dimensional data, for simplicity. For the simulations presented here, this column is taken from the closest grid point to the ignition.

Topography

Topography data was taken from the smoothed shuttle topography dataset, at 1 arc-second (approximately 30 m) resolution, downloaded from https://elevation.fsdf.org.au/.

Fuel

Fuel data was estimated from the Catchment scale Land Use Mapping data for Australia (CLUM), which was downloaded from https://www.agriculture.gov.au/abares/aclump/land-use/data-download. These

data describe the land use for the whole of Australia on an approximately 50-m grid by 3-digit numbers. The 3 digits correspond to primary, secondary and tertiary uses and are described in ABARES (2016).

These data are translated into four fuel types according to the table below, which was modified from the fuel conversion provided in example code with Spark to treat rural residential and farmland (classes 5.4.0, 5.4.2, 5.4.3, 5.4.4 and 5.4.5) as grass, rather than urban.

Primary classification	Secondary and tertiary classification	Fuel
1 (Conservation and natural environments)	All	Forest
2 (Production from relatively natural environments)	0 x	Forest
	1 x	Grass
	2 x	Forest
3 (Production from dryland agriculture and plantations)	1 x	Forest
	All other	Grass
4 (Production from irrigated agriculture and plantations)	1 x	Forest
	All other	Grass
5 (Intensive uses)	4.0, 4.2, 4.3, 4.4, 4.5	Grass
	All other	Urban
6 (Water)	All	Water

Spark configuration

Surface rate of spread was modelled as follows. Grassland and forest used the CSIRO Grasslands Model and Dry Eucalypt Model respectively (Cruz et al. 2015). The urban classification set the fire spread rate to be 0.008 times the wind speed. Spread in water was set to zero. All used the implementations in the Spark sample code for the Wangary fire (Wikipedia 2022), with the addition of a fuel mass variable.

Initial fuel mass was set to 2 kg m^{-2} (20 t ha^{-1}) in forest and urban, and 0.4 kg m^{-2} (4 t ha^{-1}) in grass. Burn rate was set to burn 0.1 kg m^{-2} per Spark time step. While the dependence on model time step here is unphysical, the fuel mass is used only for the ember transport calculations and does not have a discernable effect on the results.

Case study 1: Kilmore East Fire

This case was chosen because it is both a highly notorious and probably the best-documented case of long-range spotting in Australia, as well as being a highly significant fire with enormous impact. We previously studied this case with an implementation of the ember transport parameterisation into an earlier version of Spark (Kepert et al. 2022a). Repeating that analysis with the updated version serves as an important "reality check" on the new implementation.

The fires in southeast Australia on Black Saturday, 7 February 2009, are the worst on record in terms of lives lost, with 173 fatalities due to the direct effects (i.e., excluding the effects of smoke inhalation) of

the fires. The deadliest of these fires ignited at Kilmore East (see map in Figure 3 for locations) at about 11:45 in the morning (all times in this section are given in Australian Eastern Daylight Savings Time, 11 hours ahead of UTC) and was responsible for about 70% of the fatalities on the day. It spread rapidly to the southeast under the influence of a hot, dry, vigorous, and deep airstream, covering about 55 km in about 6 hours, before a marked wind change pushed the fire to the northeast then north. In its first 12 hours, it consumed over 100 000 ha of mostly forest and grassland. Some days later, it merged with another major fire (the Murrindindi fire) and was only extinguished after several weeks.

Cruz et al. (2012) provides a detailed reconstruction of the fire. Their analysis notes the significant role that spotting played in the rapid spread to the southeast and includes the times and locations of numerous spotfires. The farthest spotfire they analysed was 34 km from the fire front, which, after allowing for fire progression during the flight of the spot and the likely launch location, corresponded to a spotting distance analysed of 40 km. They note that these distances are similar to maximum spotting distances previously reported in similar forest types (Hodgson, 1967; Cheney and Bary, 1969; McArthur, 1969). Spotting distances of this magnitude require not just long-burning embers, but also favourable atmospheric and fire conditions. The Kilmore East fire was certainly extremely powerful, with the estimated power of up to about 2.2 TW prior to the wind change, and 8.6 TW afterwards when the north-eastern flank became the front. Although some of the spotfires were extinguished by fire crews and therefore did not contribute to fire spread, a substantial number did.

A detailed discussion of the meteorology, based on very high-resolution numerical weather prediction and Bureau of Meteorology observations, was given by Engel et al. (2012). They emphasise the deep boundary layer and strong winds ahead of the change, conditions which we favour extremely long-range ember transport in the ember transport parameterisation (Kepert et al. 2022b).

Toivenan et al. (2019) present a simulation of this day of the fire, using the coupled fire-atmosphere model, ACCESS-Fire. They were unable to obtain realistic fire spread using only the empirical fire-spread equation of McArthur (1966, 1967), with the simulated fire-run covering only about half the observed distance. When they incorporated additional ignitions based on the observed spotfire locations and times in Cruz et al. (2012), much better agreement was obtained.
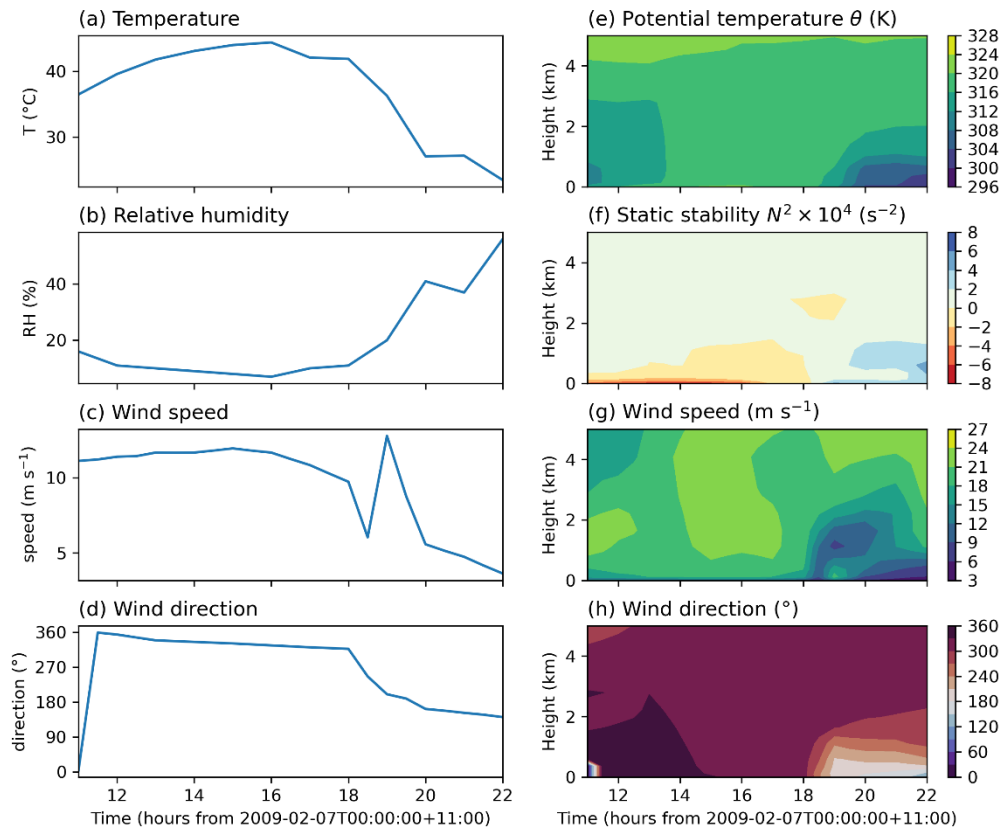
FIGURE 2: (A – D) TIME SERIES OF SURFACE METEOROLOGY FOR THE SIMULATIONS OF THE KILMORE EAST FIRE ACCORDING TO THE BARRA REANALYSIS, SHOWING RESPECTIVELY AIR TEMPERATURE, RELATIVE HUMIDITY, WIND SPEED AND WIND DIRECTION. (E – H) TIME-HEIGHT SERIES OF UPPER METEOROLOGY FOR THE SAME SIMULATIONS, SHOWING RESPECTIVELY POTENTIAL TEMPERATURE, STATIC STABILITY, WIND SPEED AND WIND DIRECTION.

Time series of the surface meteorology and time-height sections of the upper air data are shown in Figure 2. The temperature increased gradually through the day, before dropping rapidly in the lower 1 km or so of the atmosphere as the wind change arrived. The humidity was very low pre-change, increasing afterwards. Winds were strong and from the north, trending gradually towards the northwest, before turning abruptly from the southwest, tending southerly, with the change. There was a short-lived period of weak winds, followed by a pulse of strong winds, about the time of the change. The boundary layer, indicated by the layer of very low static stability, was initially about 3 km deep increasing gradually to almost 5 km during the afternoon, but a marked near-surface stable layer was prominent after the change arrived.
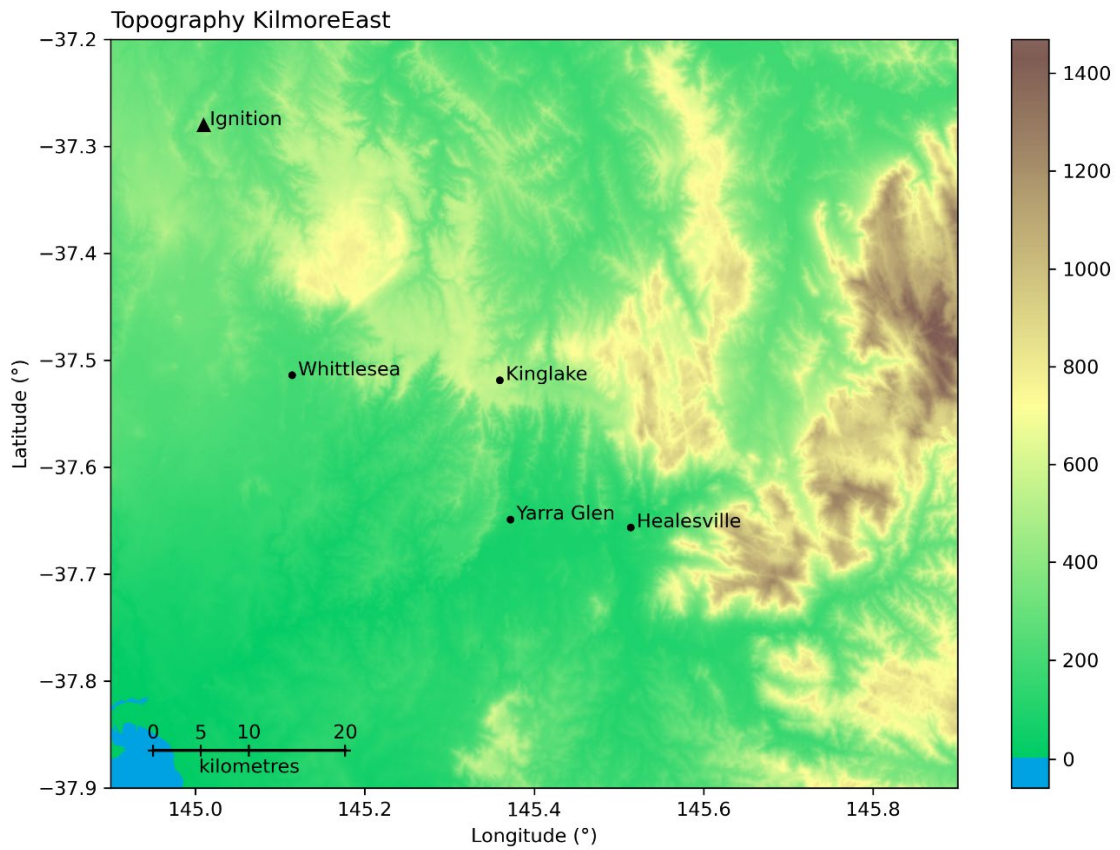
FIGURE 3: TOPOGRAPHY, IGNITION LOCATION AND PLACE NAMES FOR THE KILMORE EAST FIRE.

The topography and key place names for the Kilmore East fire are shown in Figure 3. A modest rise between the ignition point and Whittlesea affected the initial part of the fire, but much of the subsequent spread was along the low-lying area towards Yarra Glen and Healesville, until the wind change drove it up the steep slope towards Kinglake.

Kilmore East
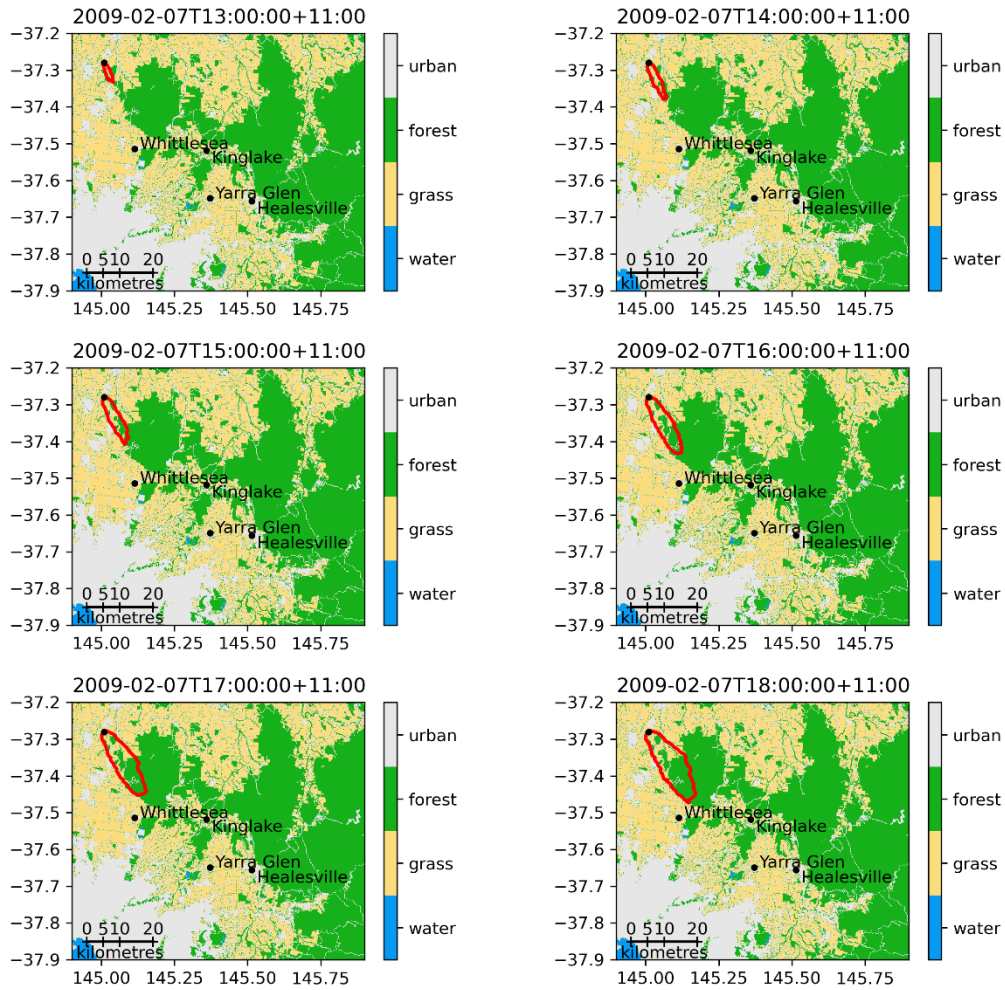
FIGURE 4: SIMULATED FIRE PROGRESSION OF THE KILMORE EAST FIRE AT HOURLY INTERVALS DURING THE AFTERNOON OF 7 FEBRUARY 2022, WITHOUT THE EFFECTS OF FIREBRAND TRANSPORT. THE RED CURVE INDICATES THE FIRE PERIMETER AND THE BLACK DOT AT ITS NORTHWEST EXTREMITY THE IGNITION POINT. COLOUR SHADING INDICATES THE ASSUMED FUEL TYPES ACCORDING TO THE COLOUR BARS.

The results of a simulation without ember transport are shown in Figure 4. The fire spreads to the southeast, reaching 24.9 km from the ignition point (a few km to the north of Whittlesea) by 6 pm when the wind change arrived. Although this was relatively rapid movement, it was nevertheless much less than observed. The area burnt reached about 150 km^2 at 6pm and 266 km^2 at 8 pm, each roughly half of Cruz et al's (2012) estimates, and peak power was about 530 GW on the wind change, less than one tenth of their estimate.

Kilmore East
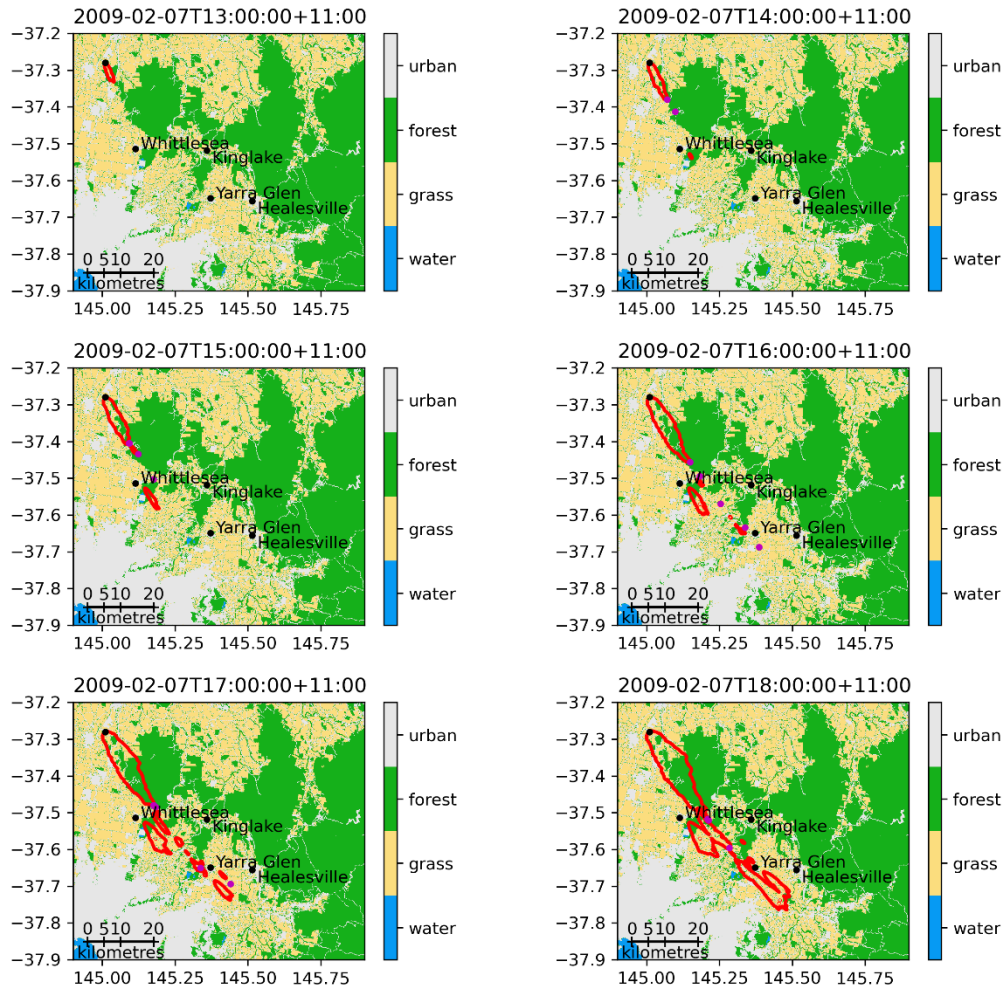
FIGURE 5: THE SAME AS IN FIGURE 4, EXCEPT INCLUDING THE EFFECTS OF FIREBRAND TRANSPORT. MAGENTA DOTS SHOW THE LOCATION OF EMBERS LAUNCHED AT THE TIME OF EACH FIGURE PANEL; NOTE THAT THEIR ACTUAL IGNITION TIMES ARE LATER BECAUSE OF TRAVEL TIME.

With spots included the fire spreads more rapidly, reaching an area of 320 km^2 at 6pm when the furthest point was 69 km from the ignition. This cumulative area and the distance travelled are both about 15% higher than the respective estimate by Cruz et al. (2012) at that time. By 8 pm, after the change, the total area had increased to 739 km^2, compared to 756 km^2 in Cruz et al. (2012).

Fire perimeters at hourly intervals through the afternoon are shown in Figure 5. A spotfire occurs in this simulation at 1:30 pm southeast of Whittlesea, with further long-range spots near Yarra Glen at 4 pm. During the latter part of the afternoon, most of the southeast portion of the fire consists of disjoint large patches, consistent with the observation by Cruz et al. (2012) that "At around 16:00 a number of subsidiary fires started by long distance spotting were spreading in forest fuels largely independent of the main zone of fire activity".

Kilmore East
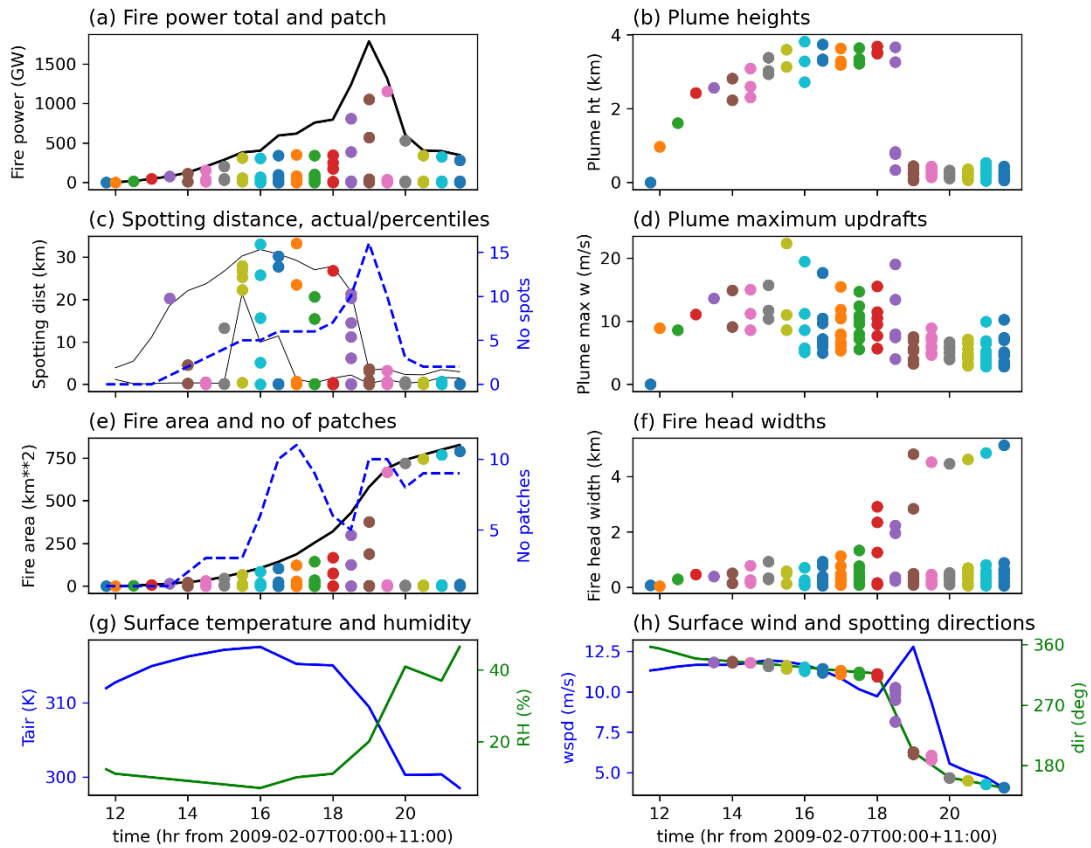
FIGURE 6: DIAGNOSTICS OF PLUME RISE AND EMBER TRANSPORT FOR THE SAME SIMULATION AS SHOWN IN FIGURE 5. (A) IS THE TOTAL FIRE POWER (BLACK CURVE) AND THAT FOR EACH FIRE PATCH (COLOURED CIRCLES). (B) SHOWS THE LEVEL OF NEUTRAL BUOYANCY FOR EACH PLUME. (C) SHOWS THE 90TH AND 50TH PERCENTILE OF TRANSPORT DISTANCE (THIN BLACK CURVES), THE ACTUAL TRANSPORT DISTANCES (COLOURED DOTS) AND THE NUMBER OF SPOTFIRES GENERATED (DASHED BLUE CURVE). (D) SHOWS THE MAXIMUM UPDRAFT OF EACH PLUME. (E) SHOWS THE TOTAL FIRE AREA (BLACK CURVE), NUMBER OF PATCHES (DASHED BLUE CURVE) AND THE AREA OF EACH PATCH (COLOURED CIRCLES). (F) SHOWS THE DIAGNOSED WIDTH OF EACH FIRE HEAD. (G) SHOWS THE SURFACE TEMPERATURE AND RELATIVE HUMIDITY, AND (H) THE SURFACE WIND SPEED AND DIRECTION) (CURVES) AND EMBER TRANSPORT DIRECTIONS (COLOURED DOTS). THE COLOURS OF THE DOTS ARE KEYED TO TIME TO FACILITATE COMPARISON BETWEEN PANELS.

Detailed diagnostics of the firebrand transport parameterisation are shown in Figure 6. Figure 6a contains the firepower, both total (black curve) and for individual fire patches (coloured dots). The peak at about 1.8 TW on the wind change is about 20% of the estimated peak of 8.8 TW by Cruz et al. (2012). Prior to the change, the intensity rose to a maximum of almost 1 TW, roughly half of the observed estimate. Diagnosed plume heights (Figure 6b) increased rapidly during the early afternoon to the range of about 2.5 – 4 km after 2 pm. The variation is due to the variation in fire power of the individual fire patches, while the rapid rise is due to the growth of the atmospheric boundary layer during the morning and early afternoon as well as the growth in buoyancy flux from the fire. The plume height decreased abruptly with the wind change, due to the increased low level static stability and the generally greater fire head widths (Figure 6f). Peak updrafts from all except the weakest plumes were above 10 m/s for most of the pre-change period (Figure 6d), more than sufficient to suspend typical bark firebrands.

The 90th percentile of spotting distance (upper thin black curve, Figure 6c) increased rapidly in the first 2 - 3 hours to above 20 km, then more slowly to 30 km. The shape of this curve is similar to that of the maximum plume height. The first spot occurred at 13:30, when the fire reached forest fuel, and happened to travel just over the 90th percentile distance at that time. There were further significant spotting distances simulated later in the afternoon. The slope of the total fire area curve increased steadily until about 7 pm, then more slowly, and the peak number of fire patches was 10 (Figure 6e). Although the simulation calculated the spotting direction as the mean wind direction to the release

height, these were close to the surface wind direction except at the time of the change, when significant directional shear existed (Figure 6h).

It is worth considering a few statements from Cruz et al. (2012) in the context of Figure 6. They note that "Between 14:15 and 14:45 partially charred fuel particles (extinct firebrands) were falling (but failing to ignite spotfires) at several locations 35–40 km SSE from where the main fire front was at the time." and "After 15:15 isolated long-range spotfires were occurring up to 30–35 km ahead of the main fire. The farthest confirmed ignitions within this period occurred in open paddocks approximately 40 km from its probable source. These isolated spotfires were quickly extinguished by fire crews." These statements are highly consistent with the rapid increase in the simulated spotting in the first few hours of the simulation, except that the maximum range simulated is a little too short.

The combination of overall too great total fire run, but spotting distance if anything too short, in this simulation raises the question of how it could be improved. It is possible that the simulated spotfire travel too fast, for several reasons. There is no representation of suppression in the simulation (Cruz et al. (2012) note active suppression between 5 pm and 6 pm), nor is there any representation of the weakened (or even reversed) wind that typically occurs downwind of a major plume. Other limitations may be that the firebrand terminal fall velocity at 6 m/s was perhaps too high, and that the number of simulated spotfires was too small or that a more sophisticated treatment of ember burnout was needed. While it is not easy to account for the first two factors in the present modelling framework, the latter are more amenable.

Kilmore East
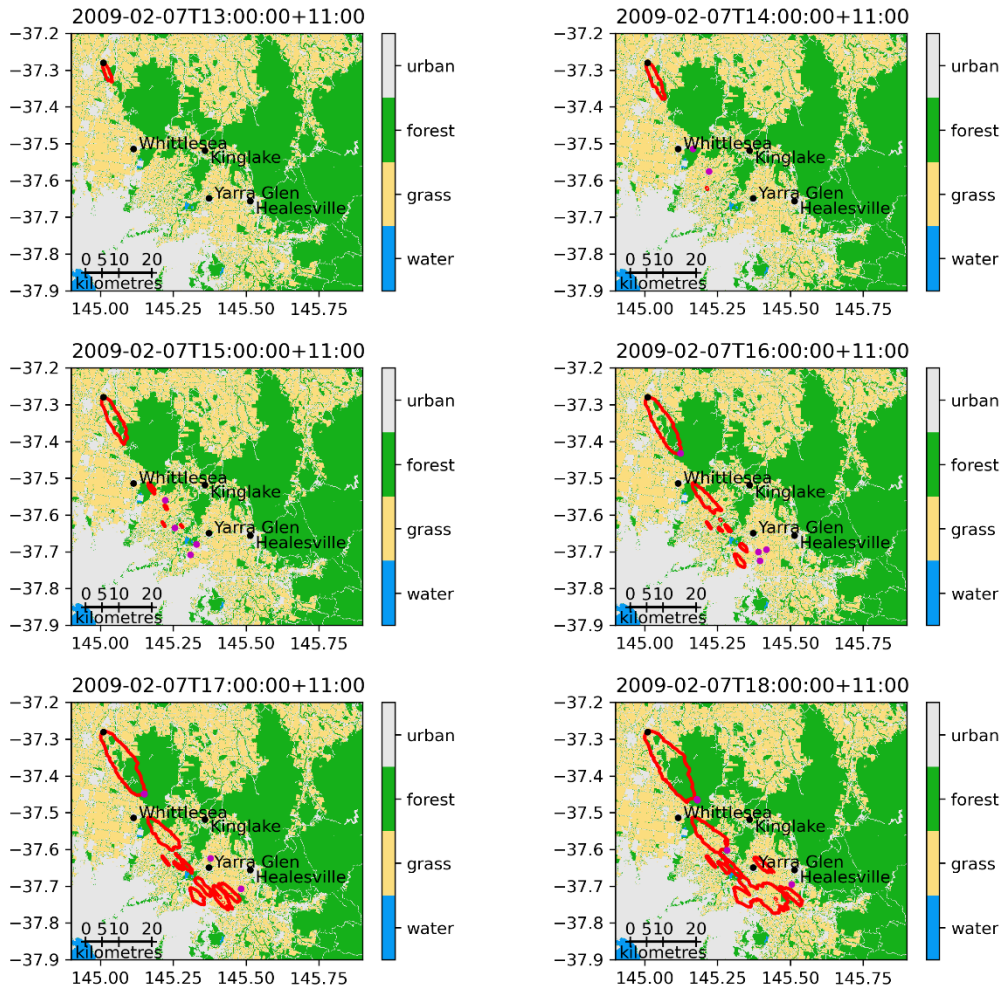
FIGURE 7: THE SAME AS FIGURE 5, EXCEPT THAT THE FALL VELOCITY HAS BEEN REDUCED TO 4 M/S.

Kilmore East
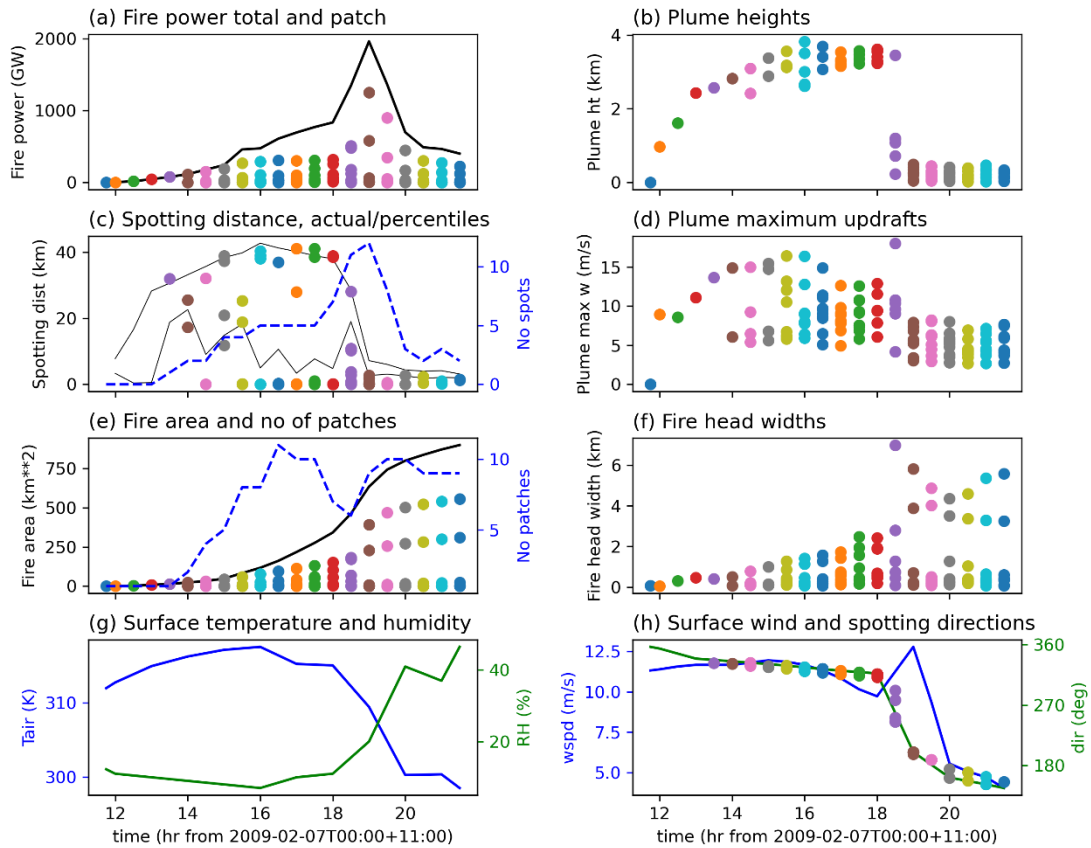
FIGURE 8: THE SAME AS FIGURE 6, EXCEPT FOR THE SIMULATION IN FIGURE 7, IN WHICH THE FALL VELOCITY WAS REDUCED TO 4 M/S.

A simulation with fall velocity to 4 m/s is shown in Figure 7 and Figure 8. The plume rise heights are very similar, although the updrafts tend to be a little weaker because of generally wider fire heads (Figure 8 b, d, f). This difference is not directly due to the fall velocity, but merely reflects different initialisation of the random number generator. The 90th percentile spotting distance increases from about 30 km to about 40 km and about 11 firebrands are transported beyond 30 km. The 50th percentile of spotting distance also increases at most times. However, despite the significant increase in long-range spotting, the overall run by 6 pm increases only by about 2 km to 71 km, with an area at that time of 342 km^2.

These differences are partly due to the model setup, but also that the ember landing positions are chosen at random from the predicted distribution. To better discern the effect of changing the fall velocity, it is necessary to account for this random element. Accordingly, we compute 50-member ensembles with both configurations. In these ensembles, only the state of the random number generator is different. Other factors containing uncertainty, including the fuels and the meteorology, are held fixed. Thus, probabilities (calculated as the ratio of the number of ensemble members experiencing a certain event to the total ensemble size) will underestimate the true uncertainty.
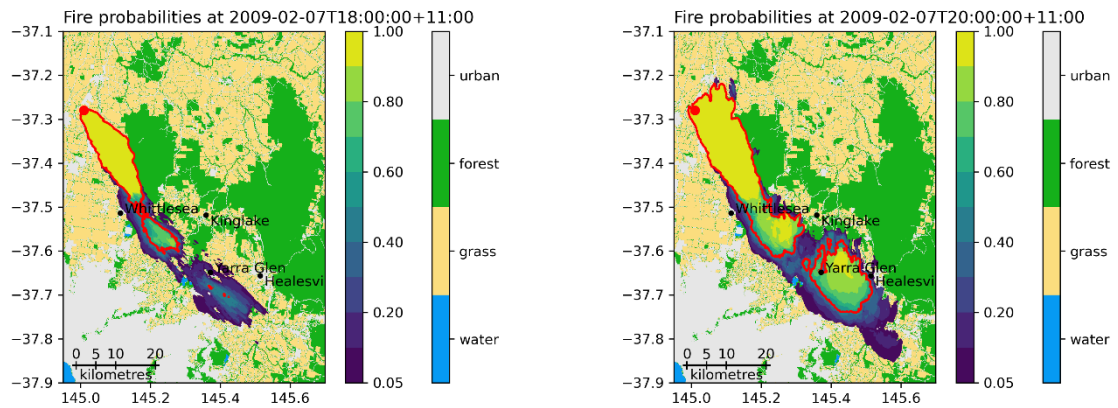
FIGURE 9: PLOTS OF FIRE PROBABILITY AT 6 PM AND 8PM, ACCORDING TO THE ENSEMBLE OF SIMULATIONS WITH A FALL VELOCITY OF 6 M/S. BLUE – YELLOW SHADING SHOWS THE PROBABILITY, AND OTHER COLOURS INDICATE FUEL TYPE. THE RED CONTOUR INDICATES THE PROBABILITY OF 0.5.
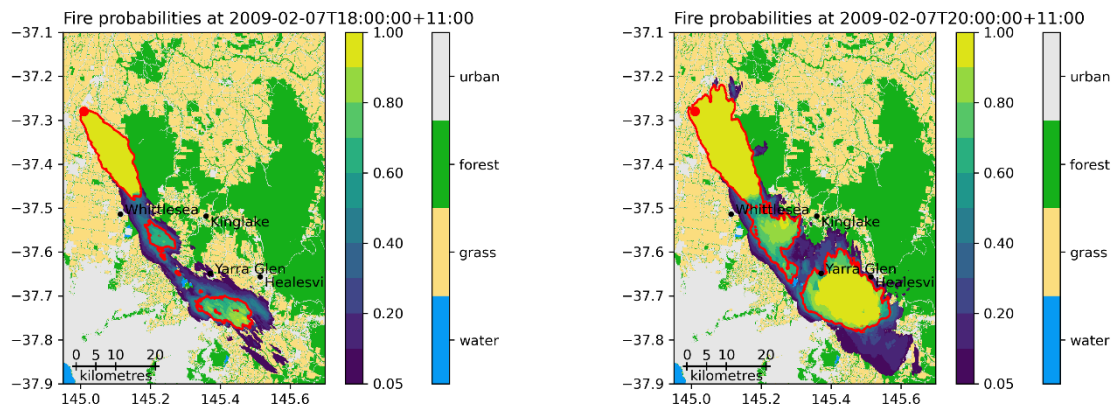
FIGURE 10: THE SAME AS FIGURE 9, EXCEPT FOR AN ENSEMBLE IN WHICH THE FALL VELOCITY WAS REDUCED TO 4 M/S.

Figure 9 maps the probability that a given location will experience fire by 6 pm and 8 pm, in the ensemble of simulations with 6 m/s fall velocity. The area burnt in the no-spot run (Figure 4) to the north of Whittlesea, which burnt in the simulation without ember transport, has a probability of 100%. A long band of lower probabilities extends to the southeast from there to a region to the south of Yarra Glen and Healesville. While the probabilities in the southernmost part of this band are mostly below 50%, most of the ensemble members simulated some fire in this region, but there was comparatively little overlap between members. Two hours later, following the wind change, these areas had grown to the northeast and now substantially overlapped, leading to a significant area of probabilities over 50%.

Similar plots for an ensemble with terminal fall velocity of 4 m/s are shown in Figure 10. The area of probable fire extends further to the southeast, because the slower-falling embers are simulated to be likely to remain in the plume for longer, and their slant trajectory after they exit the plume is more horizontal. Comparison of Figure 6c with Figure 8c shows that the 50th percentile transport distance generally increases with the slower fall velocity, and is consistent with the increase in probability to the southern extremity of the swath, and decrease near the centre, at both times shown.

Kilmore East
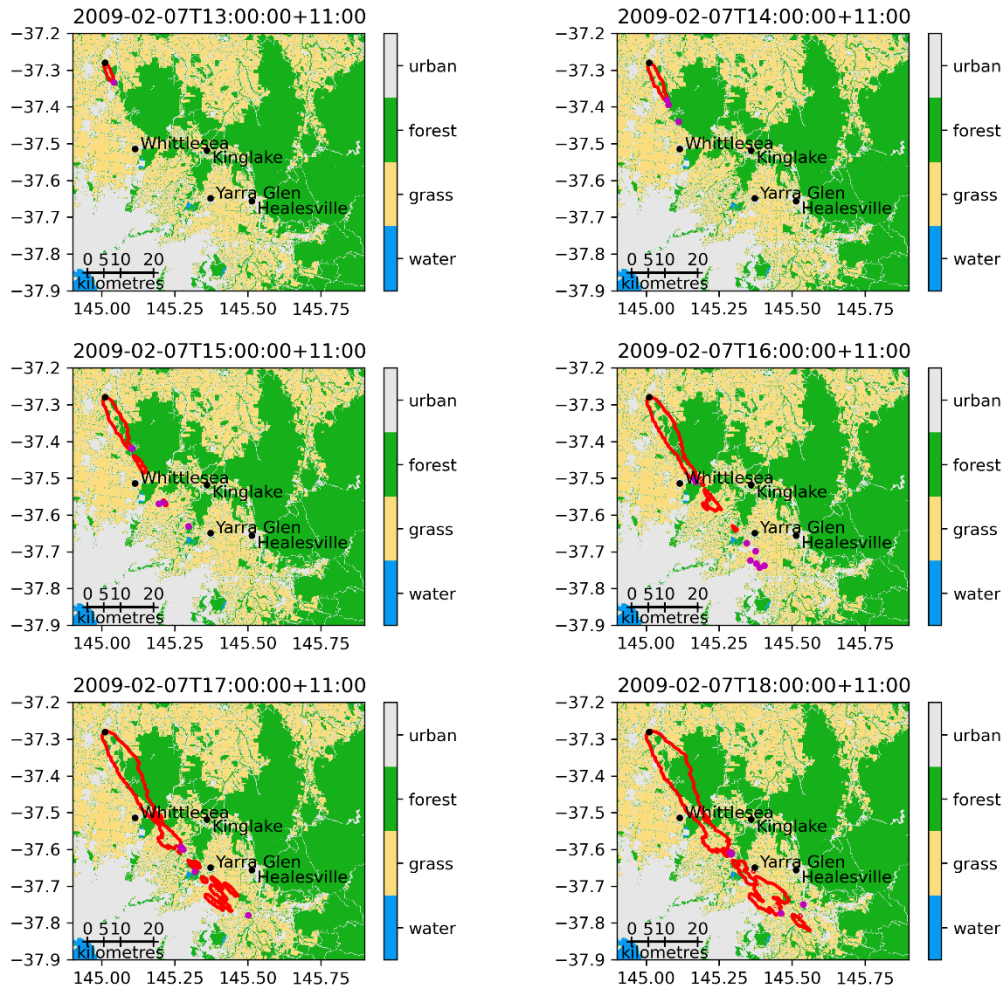
FIGURE 11: THE SAME AS FIGURE 5, EXCEPT FOR A SIMULATION IN WHICH THE RATE OF SPOTFIRE PRODUCTION IS DOUBLED.

We can similarly explore the impact of increasing the number of spotfires generated per unit mass of forest burnt. An example of a simulation is shown in Figure 11. Doubling this number creates more spotfires, without noticeably changing the distribution of spotting distance. However, the longer distances (as well as the shorter) are sampled more often. There is a tendency for the fire outline at 6 pm to be more connected, and there is also (in this case) a modest increase in total distance run and area, to 78 km and 332 km^2 respectively, at 6 pm.
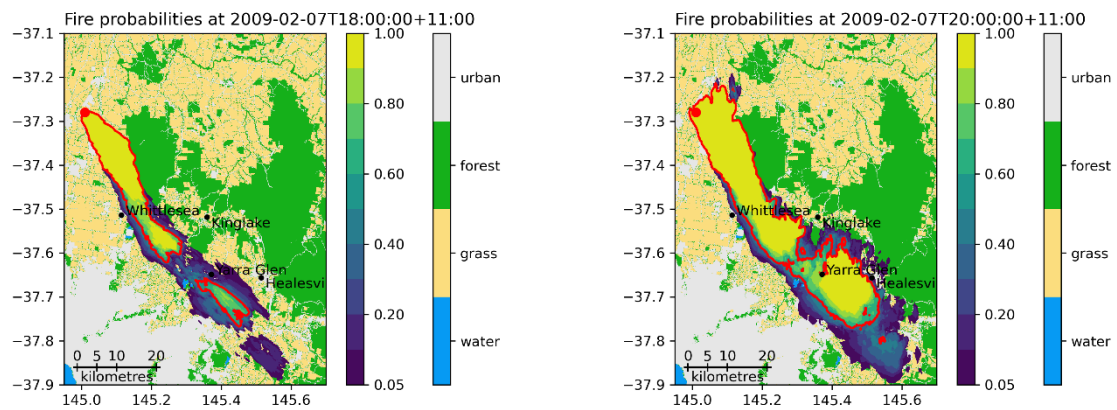
FIGURE 12: THE SAME AS FIGURE 9, EXCEPT FOR AN ENSEMBLE IN WHICH THE RATE OF SPOTFIRE PRODUCTION IS DOUBLED.

Results from an ensemble with the increased rate of spotfire production are shown in Figure 12. The most obvious difference is a substantial extension in the region of non-zero probabilities to the southeast; in fact, this is similar to the case with reduced fall velocity (Figure 10). This extension is possibly an artefact of the fact that the number of spotfires is proportional to the mass of forest burnt, rounded to the nearest integer. Previously some of the smaller spotfires well ahead of the main fire, which would have produced a number of new ignitions that rounded to 0 with the lower proportionality constant, may now round to one. There is also a general increase in probabilities throughout the swath, as expected when more spotfire ignition points are sampled from the predicted distribution. This increase is, however, less than a doubling, because some of the new ignitions fall within areas that are already burning.

The relatively small increase in the simulated fire extent in these sensitivity experiments is perhaps surprising. In the case of the source rate, it seems that there are sufficiently many spotfires generated that nearly all ensemble members sample the upper decile of the distribution at least once, and that the number of times that decile is sampled does not greatly affect the overall run. For the terminal fall velocity, it seems that the simulated plumes all have updrafts well above both the fall velocities tried, so the probability of fall-out is not strongly sensitive to the fall velocity. There would likely be greater sensitivity with weaker plumes.

Case study 2: Reedy Swamp Fire

Just after midday on 18 March 2018 a fire started within the Reedy Swamp region on the New South Wales (NSW) South Coast, Australia. Over the next several hours the fire burnt through rugged bushland, spotted across the Bega River, and impacted the coastal town of Tathra during the mid-afternoon. As a result, the town was evacuated, with 65 houses destroyed, 48 damaged, and the fire only brought under control in the overnight hours following the arrival of a cold front.

Spotting was crucial to the fire crossing the Bega River and hence reaching the town, with observed spotting distances of up to 8 − 9 km. A fuller account of the fire and comprehensive discussion of the meteorology are in Wilke et al. (2022).

Spark was configured in a similar manner to that for the Kilmore East fire. The ignition point was (36.6959°S, 149.8936°E) with a nominal radius of 100 m at midday EDST on March 18, 2022.
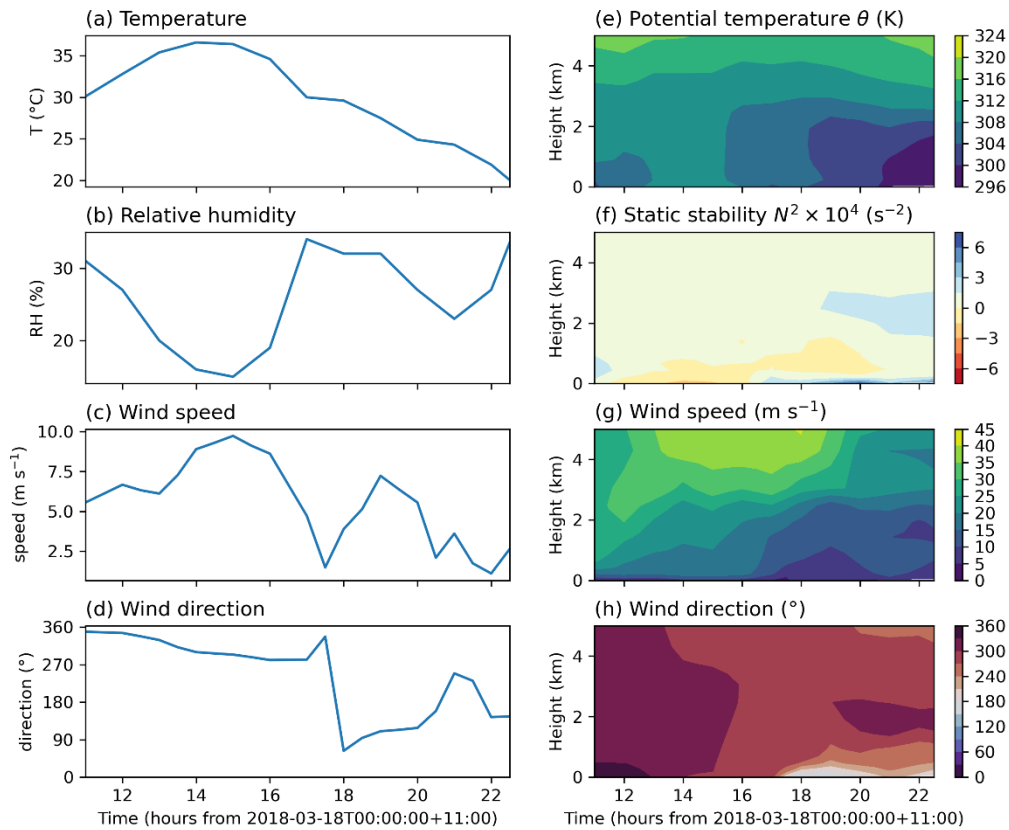
FIGURE 13: METEOROLOGICAL TIME SERIES EXTRACTED FROM THE BARRA REANALYSIS AT THE IGNITION POINT (REEDY SWAMP) OF THE TATHRA FIRE.

Meteorology was extracted from the BARRA reanalysis for both the ignition point and Tathra. The meteorology of the event was particularly complex, as analysed by Wilke et al. (2022). The time series from the ignition point features an easterly wind change rather than the southerly change, while the coastal time series featured the southerly change. This difference was because the change was confined close to the coast by the topography. The former time series are shown in Figure 13. Apart from the differences with the wind change, the two datasets are quite similar. However, the Tathra set contained some artefacts from time interpolation with the change, and the most interesting part of the fire history from a spotting perspective was prior to the change. Therefore, the simulations presented use the meteorological time series from Reedy Swamp.

Topography is shown in Figure 14. A prominent ridge lies between Reedy Swamp and the river. Much of the township of Tathra extends north from the marked location along the coast up to the river.
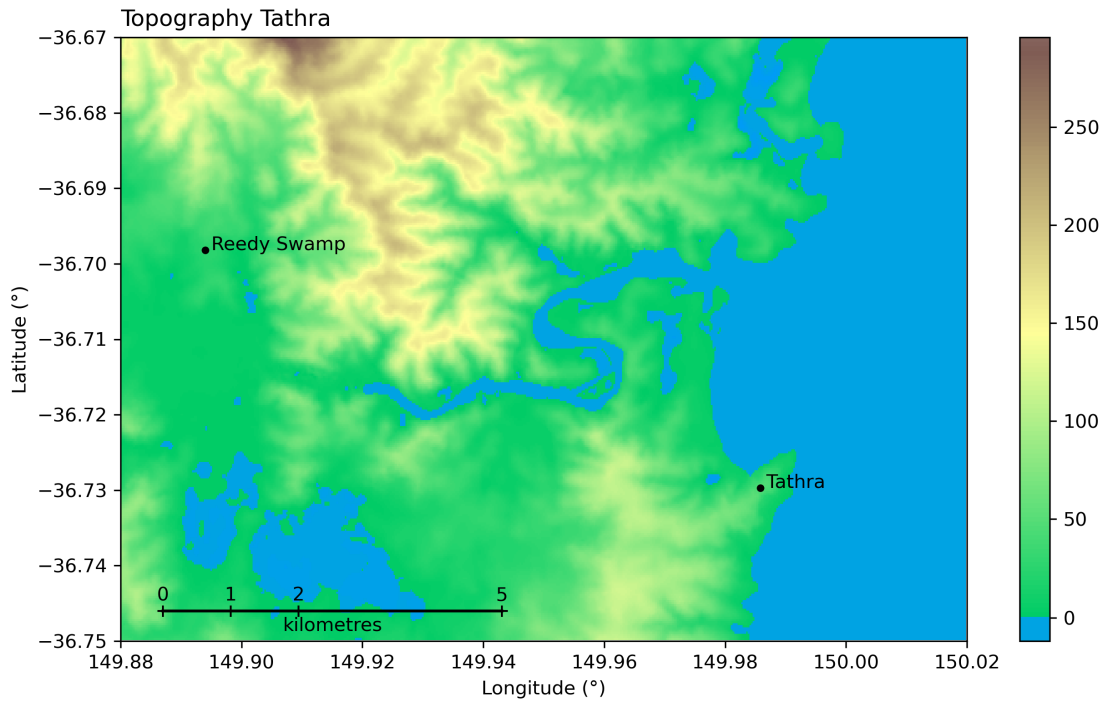
FIGURE 14: TOPOGRAPHY AND PLACE NAMES FOR THE TATHRA FIRE. THE IGNITION LOCATION WAS NEAR REEDY SWAMP.
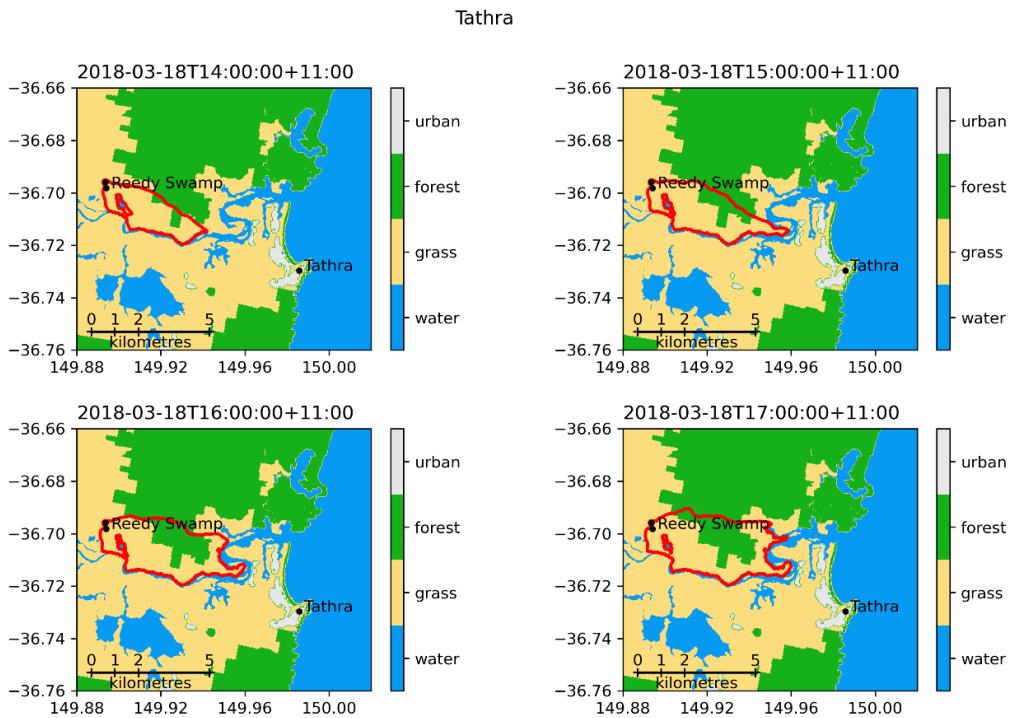
FIGURE 15: SIMULATED FIRE PERIMETERS (RED CURVES) FOR THE REEDY SWAMP / TATHRA FIRE AT TIMES AS INDICATED. SPOTFIRE PRODUCTION WAS EXCLUDED FROM THIS SIMULATION. THE IGNITION POINT IS SHOWN BY THE BLACK DOT, AND THE COLOUR SHADING SHOWS THE FUEL TYPE.

A simulation with ember transport disabled, using the Reedy Swamp meteorology, is shown in Figure 15. The simulated fire burns to the Bega River, and then along it as the wind direction tends from northwesterly to westerly. However, with spotting turned off, it fails to cross the river.

A simulation with identical fuels and meteorology, but spotting enabled, is shown in Figure 16. A couple of spotfires, one quite short-range and another landing near the coast, enable the fire to cross the Bega River by 3 pm. There were also several simulated spotfires which landed in the sea. The fire area then extends and is supplemented by additional spotfires through the afternoon, spreading into the township of Tathra. The Tathra fire is physically much smaller than Kilmore East, and the early part of the fire burnt largely fuels diagnosed as grass from the CLUM data. With the constant of proportionality between mass of forest consumed and number of spotfires set to $2 \times 10^{-7} kg^{-1}$, the value used for Kilmore East, the number of spotfires was rounded to zero. This simulation uses a value of $4 \times 10^{-6} kg^{-1}$, or 20 times higher.
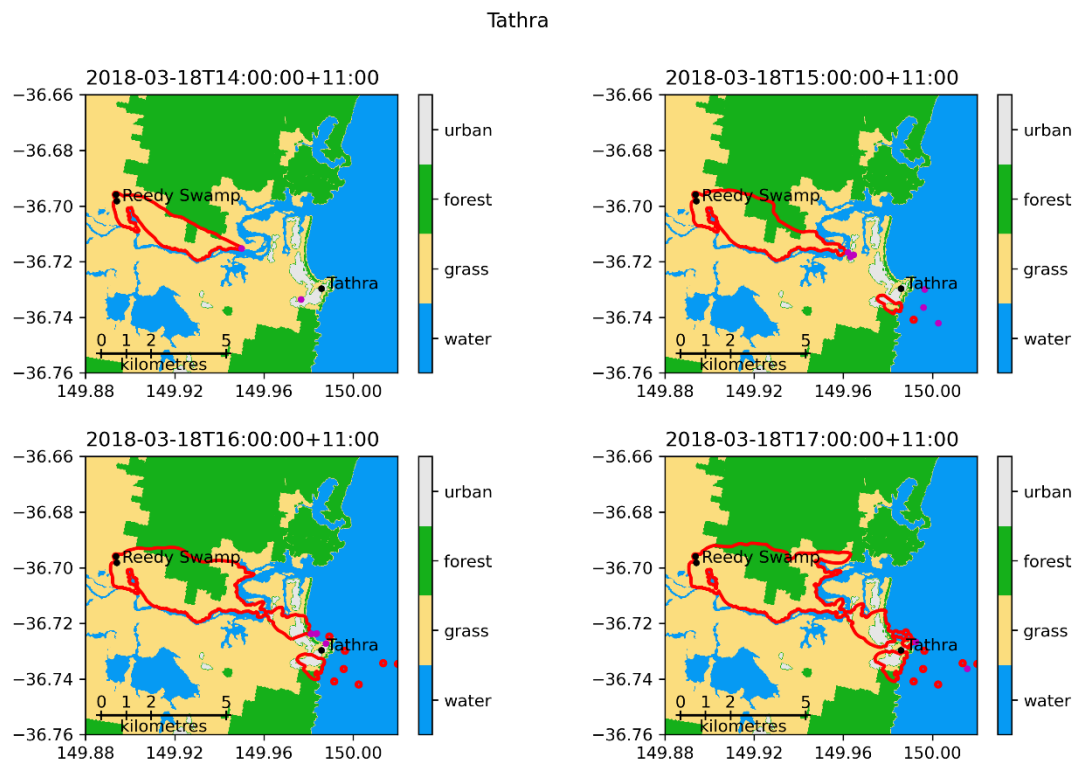
FIGURE 16: THE SAME AS FIGURE 15, EXCEPT FOR A SIMULATION WITH FIREBRAND TRANSPORT INCLUDED. THE SOURCE RATE FOR SPOTFIRES WAS SET TO 4×10^{-6} PER KG OF FOREST CONSUMED.

Fire and plume diagnostics are shown in Figure 17. The fire power varies between about 15 and 30 GW during the active period during the mid-afternoon, with plume heights mostly in the range of 1.5 to 2 km and peak updrafts from the main fire mostly around 8 to 12 m/s. Examination of detailed diagnostics of plume rise revealed that the top of the atmospheric boundary layer often limited plume rise (not shown). Being a much less powerful fire than Kilmore East in a shallower boundary layer, spotting distance is correspondingly shorter. Although the 90th percentile distance never exceeded 10 km, there was one spot at 4:00 pm of over 10 km. There were also numerous spotfires through the afternoon in the range of 3 to 8 km. Many of the new "spotfires" landed in the ocean and did not spread, however Spark retained them as non-spreading fires and so the diagnosed number of patches in this figure is not accurate.

An ensemble of simulations was generated in a similar manner to that for the Kilmore East fire. Neither the meteorology nor fuels were perturbed, with the sole source of ensemble spread being the sampling from the distribution of landing positions. Fire probabilities computed from this ensemble at 3 pm and 5 pm are shown in Figure 18. At 3 pm, a substantial area to the south of the river, fringing on the town of Tathra, has probability of fire of up to about 0.5. By 5 pm, this area has extended northwards into the town, with the southern part of the town now covered by probabilities of over 0.5.

Tathra
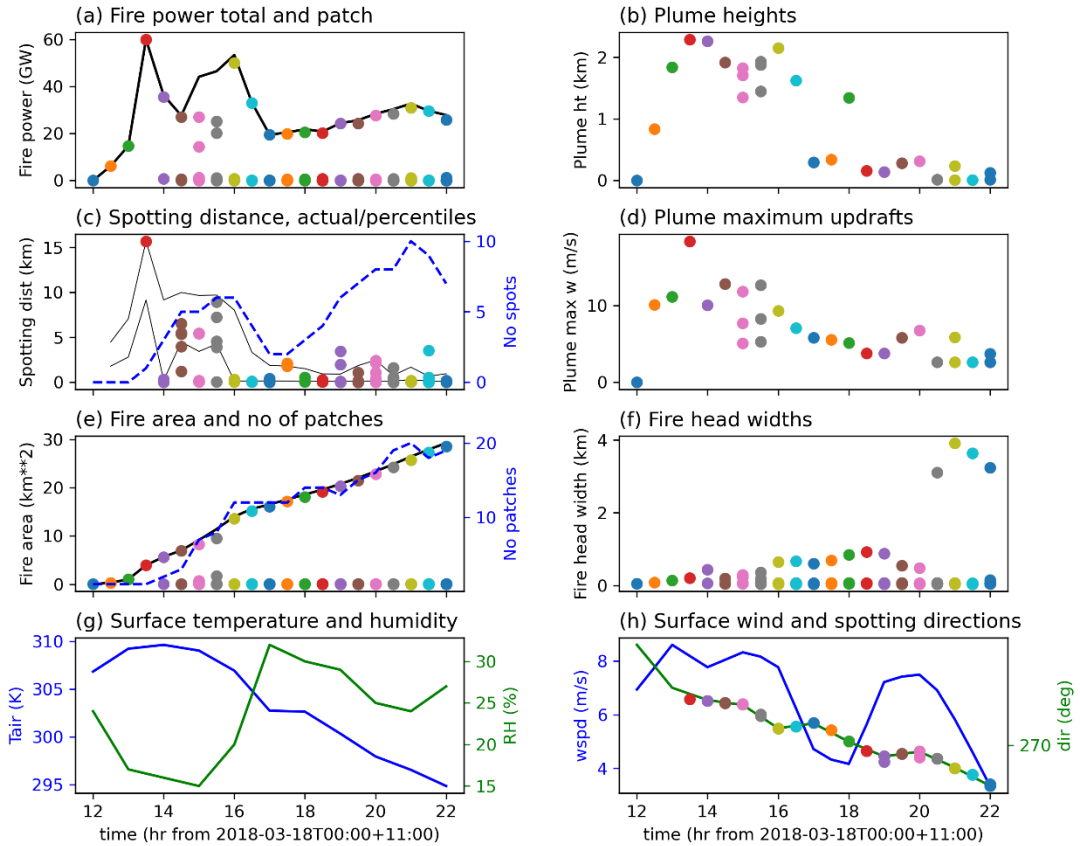
FIGURE 17: DIAGNOSTICS OF PLUME RISE AND EMBER TRANSPORT FOR THE SAME SIMULATION AS SHOWN IN FIGURE 16. (A) IS THE TOTAL FIRE POWER (BLACK CURVE) AND THAT FOR EACH FIRE PATCH (COLOURED CIRCLES). (B) SHOWS THE LEVEL OF NEUTRAL BUOYANCY FOR EACH PLUME. (C) SHOWS THE 90TH AND 50TH PERCENTILE OF TRANSPORT DISTANCE (THIN BLACK CURVES), THE ACTUAL TRANSPORT DISTANCES (COLOURED DOTS) AND THE NUMBER OF SPOTFIRES GENERATED (DASHED BLUE CURVE). (D) SHOWS THE MAXIMUM UPDRAFT OF EACH PLUME. (E) SHOWS THE TOTAL FIRE AREA (BLACK CURVE), NUMBER OF PATCHES (DASHED BLUE CURVE) AND THE AREA OF EACH PATCH (COLOURED CIRCLES). (F) SHOWS THE DIAGNOSED WIDTH OF EACH FIRE HEAD. (G) SHOWS THE SURFACE TEMPERATURE AND RELATIVE HUMIDITY, AND (H) THE SURFACE WIND SPEED AND DIRECTION) (CURVES) AND EMBER TRANSPORT DIRECTIONS (COLOURED DOTS). THE COLOURS OF THE DOTS ARE KEYED TO TIME TO FACILITATE COMPARISON BETWEEN PANELS.

FIGURE 18: PLOTS OF FIRE PROBABILITY AT 3 PM AND 5PM FOR THE REEDY SWAMP / TATHRA FIRE, ACCORDING TO THE ENSEMBLE OF SIMULATIONS. BLUE – YELLOW SHADING SHOWS THE PROBABILITY, AND OTHER COLOURS INDICATE FUEL TYPE. THE RED CONTOUR INDICATES THE PROBABILITY OF 0.5. PROBABILITIES OVER THE SEA INDICATE FIREBRAND LANDING POSITIONS.

Following the brief period of spotting to 15 km, for about 2 hours the 90th percentile spotting distance is around 9 to 10 km. This latter distance is in excellent agreement with the observed maximum spotting distance of 8 – 9 km noted in Wilke et al. (2022). The timing of the impact on the town is also consistent with the simulations, although we note that the subsequent northwards spread is underestimated due to the use of wind direction data from the ignition point. Wilke et al. (2022) note that the fire spotted across the river at 2:56 pm, began to impact the town at 15:34 pm and reached the coast at 16:27, with at least

50 houses alight by 17:29. The corresponding timings naturally vary between members in our ensemble, but the observed values fall within the ensemble envelope.

Case study 3: Timbarra Fire

This fire has not been documented in the publicly available literature. I am grateful to Musa Kilinc for generously providing the reconstruction data plotted in this report, and for very helpful discussions about the circumstances of the fire.

The Timbarra fire commenced on 16 January 2019 near 37.25°S 148.02°E, about 25 km to the north-northeast of Timbarra, Victoria. Spread was slow until the 25th when it took a major run to the southeast. The topography of the region is shown in Figure 19. The ignition point was high on a long, generally downwards slope to the south and east. The deepest valley is the Snowy River, with several other north-south valleys crossing the fireground.
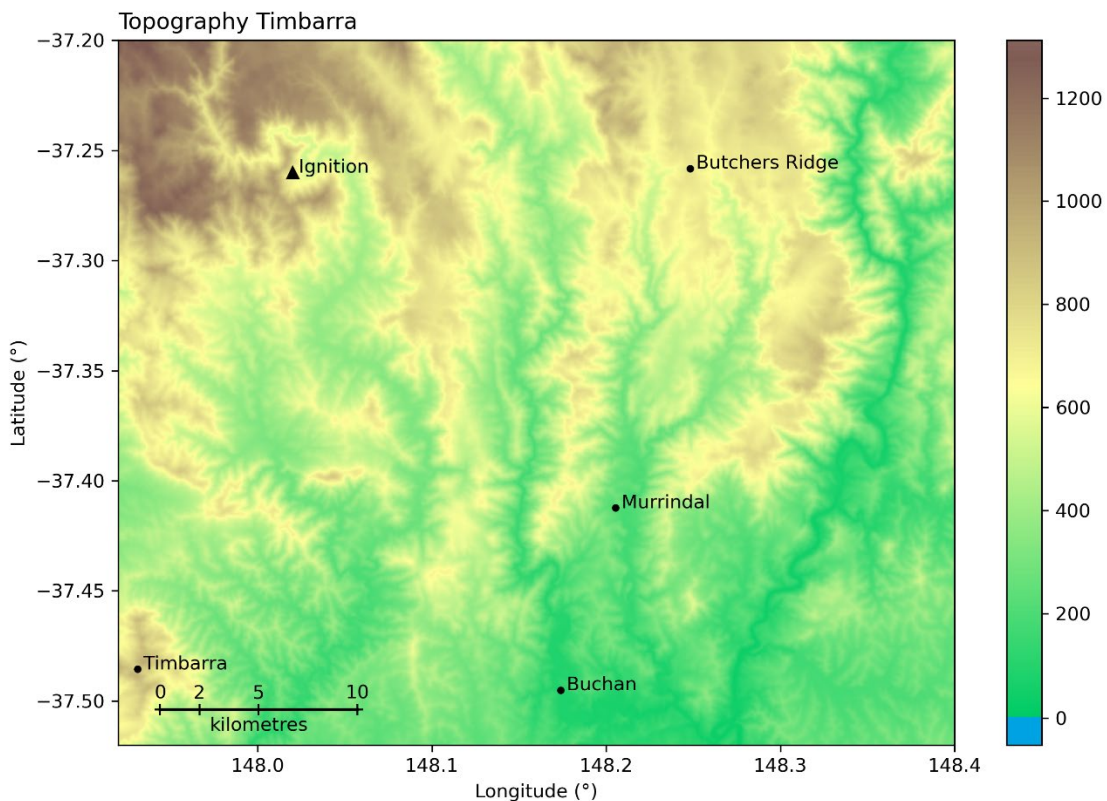
FIGURE 19: TOPOGRAPHY FOR THE TIMBARRA FIRE. THE APPROXIMATE LOCATION OF THE IGNITION POINT IS SHOWN IN THE TOP LEFT OF THE FIGURE.

Meteorological data for this period, from the BARRA reanalysis, are shown in Figure 20. According to the reanalysis, it was a hot, dry day, with the temperature exceeding 30°C at 9 am and 40°C for several hours in the afternoon. The wind direction was west-northwesterly initially, slowly tending more westerly, before a shallow change in the early evening. The wind speed was not especially strong at the surface, steadily decreasing from about 6 m/s (22 km/hr) until the change, but a marked low-level jet was apparent about 500 m above the surface in the morning, gradually lifting and weakening during the day. Similar low-level jets, including on lee-slope topography, have been discussed in severe fire events by Kepert and Fawcett (2013), Peace et al. (2017, 2022), and Wilke et al. (2022). A shallow nocturnal inversion eroded during the morning, with the boundary layer depth growing to reach about 3 km by mid-afternoon.
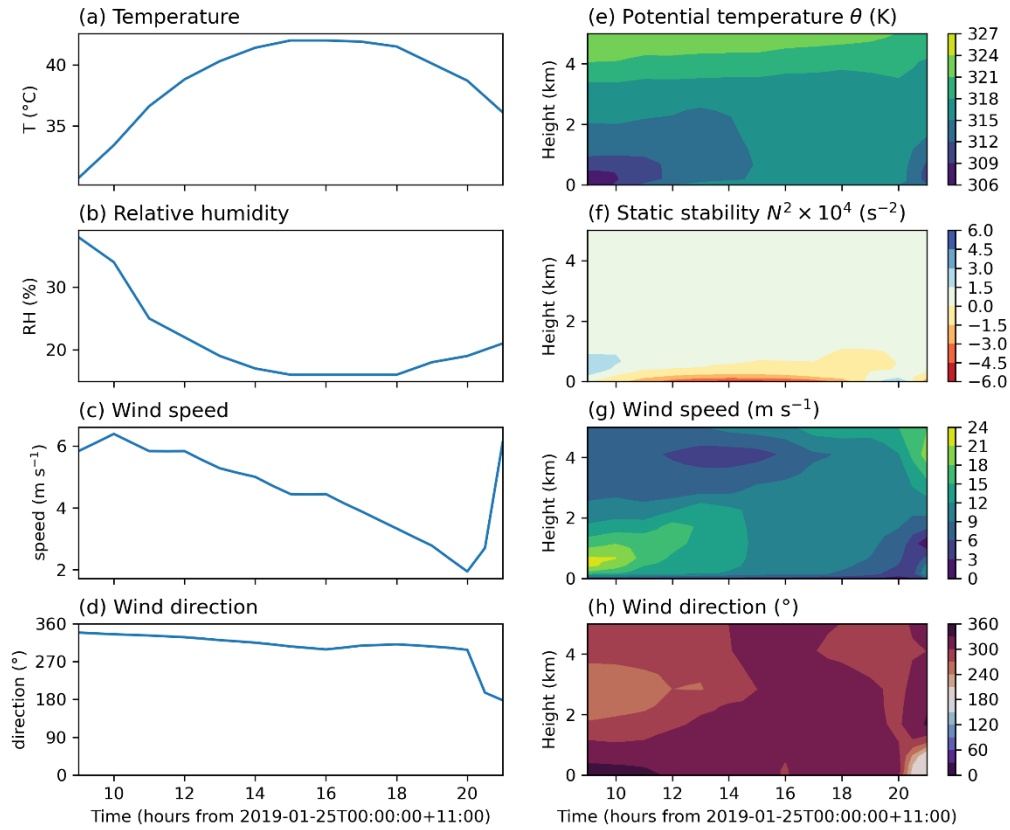
FIGURE 20: (A – D) TIME SERIES OF SURFACE METEOROLOGY FOR THE SIMULATIONS OF THE TIMBARRA FIRE ACCORDING TO THE BARRA REANALYSIS, SHOWING RESPECTIVELY AIR TEMPERATURE, RELATIVE HUMIDITY, WIND SPEED AND WIND DIRECTION. (E – H) TIME-HEIGHT SERIES OF UPPER METEOROLOGY FOR THE SAME SIMULATIONS, SHOWING RESPECTIVELY POTENTIAL TEMPERATURE, STATIC STABILITY, WIND SPEED AND WIND DIRECTION.

The observed fire progression on that day is summarised in Figure 21. Early in the morning, the fire perimeter had an unusual shape due to a backburn that anticipated the more severe conditions of that day (Figure 21a). The first recorded spotfire, about 2 km ahead of the main front at about 11:02 (Figure 21b), preceded a notable outbreak that led to a rapid spread to the southeast (Figure 21c). Spotting to similar distances continued to be a feature until around 13:41 when a single spotfire was observed some 9 km east-southeast from the main front (Figure 21d). Some broadening of the fire followed with further progression and further shorter-range spotting (Figure 21e), which continued into the early evening (Figure 21f).
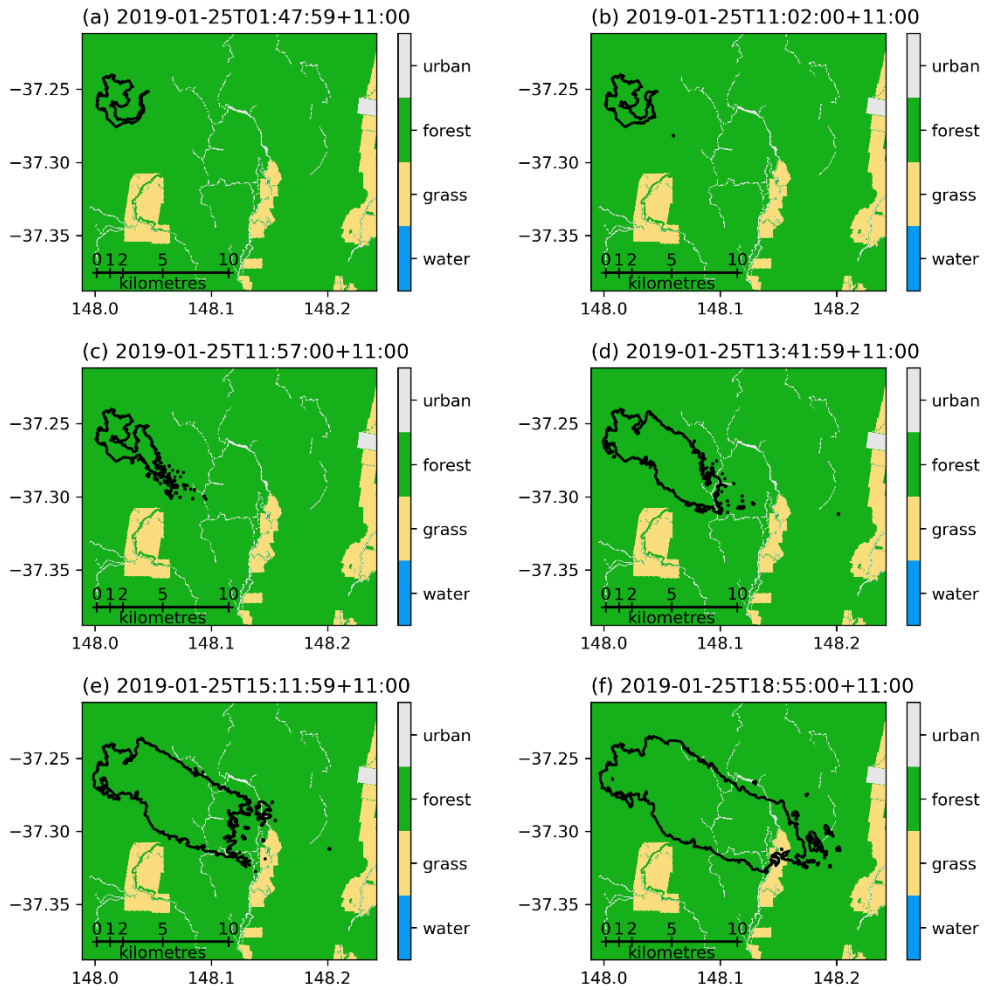
FIGURE 21: PROGRESSION OF THE TIMBARRA FIRE ON 25 JANUARY 2019. THE COLOUR SHADING SHOWS THE SIMPLIFIED FUEL MAP USED FOR THE SIMULATION AND IS INTENDED AS A VISUAL REFERENCE. TIMES ARE INDICATED ABOVE EACH PANEL. FIRE DATA COURTESY OF MUSA KILINC.

A simulation of the fire, with the firebrand transport parameterisation turned off, is shown in Figure 22. To reflect the fact that the fire had burnt for several days prior to this simulation commencing, the initial perimeter was approximated by a circle of radius 500 m, rather than 100 m as in the other experiments, centred on 37.26°S 148.02°E. The fire grew steadily to the southeast, but the length at 7 pm was about 10 km, in contrast to 16 km in the reconstruction.

Timbarra
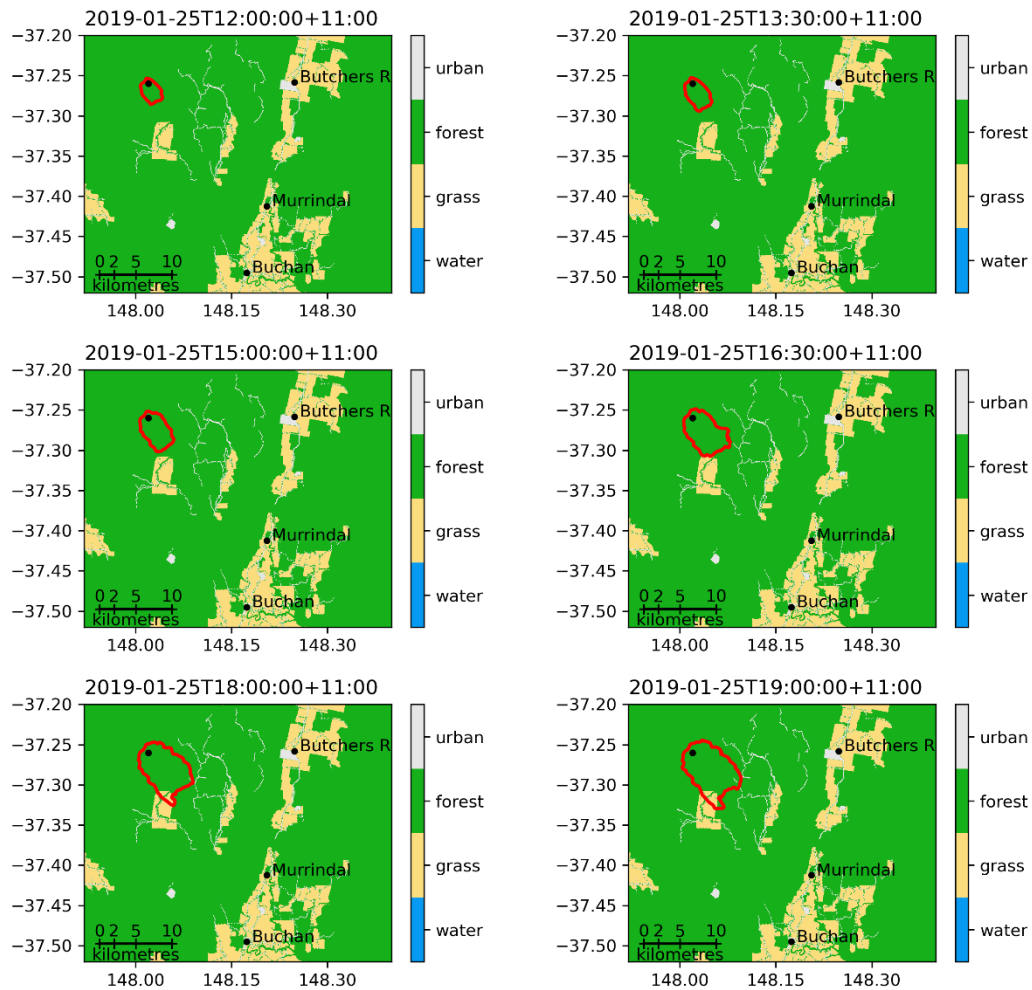
FIGURE 22: SIMULATED FIRE PROGRESSION FOR THE TIMBARRA FIRE, WITH THE FIREBRAND TRANSPORT PARAMETERISATION OMITTED. THE IGNITION POINT IS SHOWN BY THE BLACK DOT, AND THE FIRE PERIMETER AT 90-MINUTE INTERVALS BY THE RED CURVES.

A simulation with spotting included is shown in Figure 23, and the plume and fire diagnostics for that simulation in Figure 24. Spotting commenced in this simulation at 1 pm, prior to which the rate of forest fuel consumption was insufficient to generate embers (the standard constant of proportionality, $2 \times 10^{-7} kg^{-1}$ was used). Between 2 pm and 4 pm, 3 long-range spots of more than 10 km were generated, and the potential for spots to this range existed for about an hour before they occurred. All were from the upper end of the calculated distribution function, making this an unusual event. Their landing points were near the single observed long-range spot (Figure 21d). While further spots were generated after these three, they all came from the short-range end of the distribution.

The evolution of the fire and plume was broadly similar to the other events. Spread was very slow, and the fire power low, until after sunrise. Plume rise and spotting potential were negligible overnight. During the morning, the fire became more intense with the warmer, drier air, and the additional heat flux, combined with the deepening atmospheric boundary layer, allowed the plume height to steadily increase to about 1.5 km by midday and almost 3 km by late afternoon. The plumes from the spotfires, although having only a fraction of the heat flux, were simulated to rise to only a little lower, aided by their narrower geometry and hence smaller initial radius.

An ensemble simulation with the same settings is shown in Figure 25. At 3:30 pm, a mix of short and long-range spotting is evident. The former is shown by the fringe of blue on the southeast edge of the main fire area, where spotfires have enabled some ensemble members to progress slightly further. The longer-range spotting is evidenced by the few patches of blue along a line to the southeast, up to about 12 km ahead of the main area of fire probabilities at 3:30 pm. By 6 pm, the few patches to the southeast have coalesced into an extended band of probabilities of up to about 40%, along with one isolated patch further to the southeast, possibly reflecting that a spotfire in one ensemble member had become vigorous enough to create a second-generation spotfire.
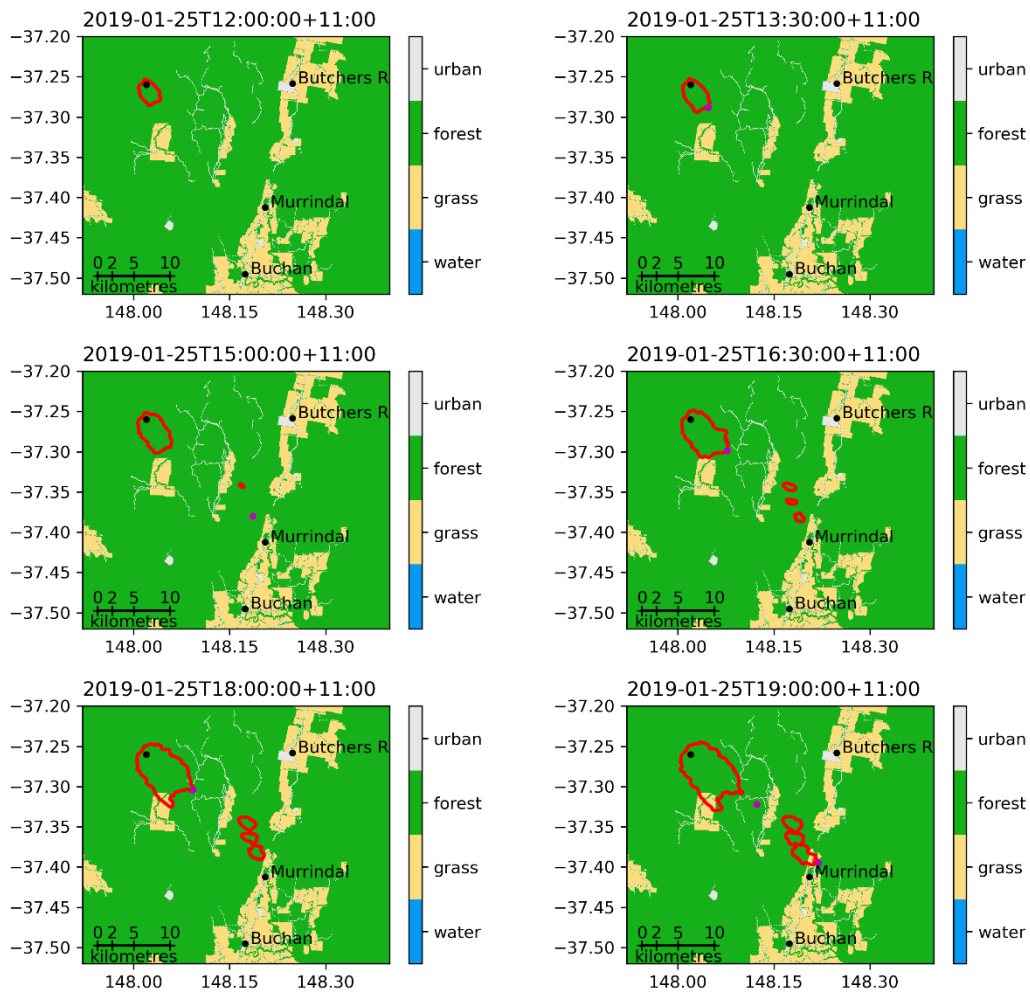
FIGURE 23: THE SAME AS FIGURE 22, EXCEPT WITH SPOTTING INCLUDED. MAGENTA DOTS SHOW THE LOCATION OF SIMULATED SPOTFIRES, PLOTTED AT THE TIME OF THEIR LAUNCH.

Timbarra
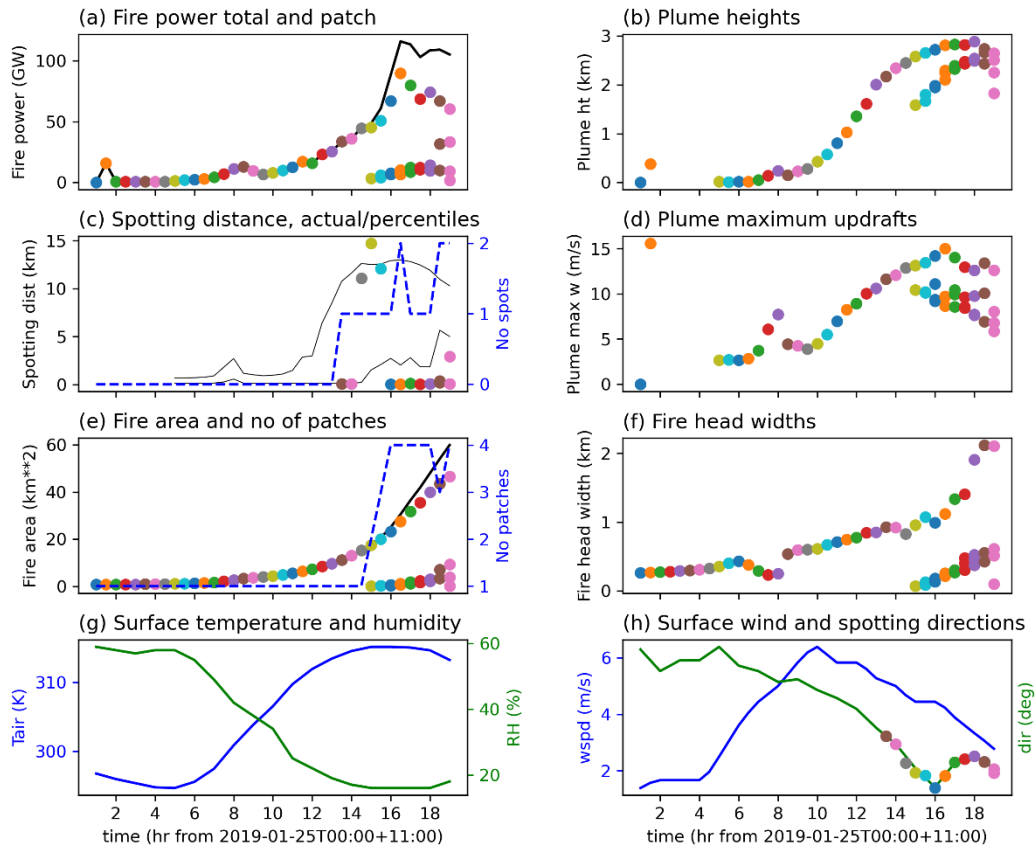
FIGURE 24: DIAGNOSTICS OF PLUME RISE AND EMBER TRANSPORT FOR THE SAME SIMULATION AS SHOWN IN FIGURE 23. (A) IS THE TOTAL FIRE POWER (BLACK CURVE) AND THAT FOR EACH FIRE PATCH (COLOURED CIRCLES). (B) SHOWS THE LEVEL OF NEUTRAL BUOYANCY FOR EACH PLUME. (C) SHOWS THE 90TH AND 50TH PERCENTILE OF TRANSPORT DISTANCE (THIN BLACK CURVES), THE ACTUAL TRANSPORT DISTANCES (COLOURED DOTS) AND THE NUMBER OF SPOTFIRES GENERATED (DASHED BLUE CURVE). (D) SHOWS THE MAXIMUM UPDRAFT OF EACH PLUME. (E) SHOWS THE TOTAL FIRE AREA (BLACK CURVE), NUMBER OF PATCHES (DASHED BLUE CURVE) AND THE AREA OF EACH PATCH (COLOURED CIRCLES). (F) SHOWS THE DIAGNOSED WIDTH OF EACH FIRE HEAD. (G) SHOWS THE SURFACE TEMPERATURE AND RELATIVE HUMIDITY, AND (H) THE SURFACE WIND SPEED AND DIRECTION) (CURVES) AND EMBER TRANSPORT DIRECTIONS (COLOURED DOTS). THE COLOURS OF THE DOTS ARE KEYED TO TIME TO FACILITATE COMPARISON BETWEEN PANELS

FIGURE 25: PLOTS OF FIRE PROBABILITY AT 3:30 PM AND 6PM FOR THE TIMBARRA FIRE, ACCORDING TO THE ENSEMBLE OF SIMULATIONS. BLUE – YELLOW SHADING SHOWS THE PROBABILITY, AND OTHER COLOURS INDICATE FUEL TYPE. THE RED CONTOUR INDICATES THE PROBABILITY OF 0.5.

These simulations contain some encouraging elements. The timing and distance of spotting near 10 km are consistent with, but perhaps a little later than, the single observed spot to similar range. In addition, there were reports of ash falling almost to Orbost, some 50 km away (Musa Kilinc, personal communication). However, there are also some significant discrepancies. That observed long-range spotfire was much slower to grow than those simulated, possibly because it landed in an area where a recent fire had reduced the fuel load (Musa Kilinc, personal communication). In addition, there was a

profusion of observed spotfires in the range of $1 - 2$ km, while the simulated spots of relatively short range tended to be close to the modelled fire perimeter.

The no-spot simulation shown here ran at about 2/3 the observed rate, while those with spotting enabled gave a more realistic indication of the spread potential. We caution, however, that this result does not demonstrate that long-range spotting was the cause of the greater than simulated spread. Indeed, the one observed long-range spot contributed little to the fire spread. One possible reason is the simple fuel data used here. A possible alternate cause could be the absence of fire-atmosphere interactions in these simulations. We have previously simulated cases using the couple fire-atmosphere model, ACCESS-Fire, where the atmosphere featured a low-level jet, as found during the morning here. The interaction between the fire and the atmosphere was apparently able to bring the greater momentum in the jet down to the head of the fire, such that the head-fire experienced stronger winds and thereby more rapid spread than was found in an uncoupled simulation. Obviously, we cannot test this hypothesis in the present modelling setup. However, we suggest it would be an interesting candidate for study with ACCESS-Fire.

5 Discussion

We have presented simulations of three fires with the Spark fire simulator coupled to the firebrand transport parameterisation described by Kepert et al. (2022a,b). The predicted maximum transport distances vary dramatically between these simulations, with the depth of the atmospheric boundary layer, and its impact on plume rise, being a substantial contributor to these differences. In the case of the Kilmore East, Tathra and Timbarra fires, the predicted 90th percentile spotting distances are in good agreement with observations.

Ensemble simulations were prepared for each of these fires. These exhibited a fair degree of spread between members, due to the part of the firebrand transport method that utilises a random number generator to sample from the predicted distribution of landing points. However, sufficient firebrands were generated to produce a few in the upper decile of distance for nearly all fires, with the result that all fires produced a significant increase in fire spread, power, and area burnt than simulations with spotting excluded.

The extreme spotting distance observed in the Kilmore East fire (Cruz et al. 2012) raises the question of what factor, or factors, contributed to this event. We conclude that the following were important:

- An intense fire. However, we note that most of the simulated plumes, whether from the main fire or from weaker spotfires, showed substantial transport potential. We conclude that this fire, with an estimated pre-change power output that peaked at over 2 TW, was more than intense enough to loft embers this far.

- A relatively narrow fire front prior to the change, implying a strong, deep updraft to the plume.

- A deep atmospheric boundary layer, so that the ember drop height is as high as possible and the descending part of the ember trajectory is long.

- Strong winds to transport the embers along.

- Long-burning firebrands, to allow for transport times of half an hour or more.

- A receptive landing zone, to ensure that firebrands cause sustained ignitions.

Of these six factors, the first two pertain to the fire, the next two to the meteorology on the day, and the final two to the fuels.

The two meteorological factors, a deep atmospheric boundary layer and strong winds, were also present in the other two cases, but not to the same degree. It is notable that Cruz et al.'s (2012) reconstruction of the Kilmore East fire notes that the spotting reduced to much shorter distances following the wind change and the increase in near-surface static stability, even though the fire power reached its peak of 8.6 TW at this time. These meteorological factors should be predictable several days or more in advance with current technology, opening the possibility of providing an early warning of days with high spotting potential.

For the Tathra fire, spotting was a necessary element for the crossing of the Bega River and the subsequent impact on the town. The simulations with and without spotting enabled captured this difference well, provided that the rate at which spotfires were generated, here expressed as being proportional to the mass of forest burnt, was substantially increased. While the constant of proportionality here includes not just the production of embers, but also their probability of not burning out in flight and landing in a fuel zone conducive to a sustained ignition, choosing an appropriate value for the proportionality constant remains a difficult process.

The no-spotting simulation of the Timbarra fire underpredicted the spread of the fire, while including spotting led to greater spread. We cannot, however, state unequivocally that spotting is the main cause

of the underprediction in this case. The meteorology indicates a strong low-level jet through much of the morning, and studies of other events with coupled fire-atmosphere models have shown that the momentum from such jets can be transported downwards to the head of the fire and increase the rate of spread. In addition, the observed long-range spotfire, of about 9 km, was very slow to spread and did not appear to contribute strongly to the observed spread of the fire.

6 Outstanding questions

Several components of this work have required the application of a degree of judgement to the solutions chosen. Some well-directed research will substantially improve either confidence in their accuracy, or alternatively suggest improvements. Particular issues are as follows.

The plume rise and strength depend on the fire characteristics. The crucial parameters are fire power (or buoyancy flux) and the equivalent size. Much of the theory of plume rise is for compact, near-circular sources. Determining an equivalent plume source radius from a natural, irregular fire, with a substantial variation in heat flux across the fire ground, is not easy.

The firebrand source function. We have insufficient information on how fast embers are produced from various forest types, their composition, and terminal fall velocity. For the Tathra fire, we had to use a much higher production rate than in the other two, for no readily apparent reason. Other complicating factors are that at the present state of development, this formation rate has folded into it the probabilities of not burning out in flight and of producing sustained ignition on landing.

Modelling firebrand burnout. Valuable papers on the burning characteristics of bark firebrands from eucalyptus and other species include Ellis (2013) and Hall et al. (2015). The latter reports a maximum burnout time of over 20 minutes, consistent with that implied by the observed spotting distances in the Kilmore East fire. Inevitably, burnout time will be a distribution, in many cases with a long tail to the long-burning end. How to statistically model this distribution is an open question. The exponential distribution is likely a reasonable first choice, although more generality may require members of the gamma family. However, the transport parameterisation includes in its output an estimate of travel time, so accounting for in-flight burnout in the model will be straightforward.

Firebrand ignition. At present, all firebrands are assumed to ignite. In reality, this will depend on (at least) the fuel characteristics in the landing zone and any suppression activities. It is also necessary to account for the time taken for a new ignition to become a well-developed fire.

Some, and perhaps all, of the above factors constitute further reasons to utilise an ensemble approach in simulations of this nature.

References

1   ABARES, 2016: The Australian Land Use and Management Classification Version 8. Downloaded from http://data.daff.gov.au/data/warehouse/9aal/2016/alumc9aal20161017/AustLandUseMgtClassfnVersion8_v1.0.0.pdf, 12 March 2019.

2   Cheney, N.P. and Bary, G.A.V., 1969: The propagation of mass conflagrations in a standing eucalypt forest by the spotting process. *T. T. C. P. Mass Fire Symposium*, Canberra February 1969.

3   Cruz, M.G., A.L. Sullivan, J.S. Gould, N.C. Sims, A.J. Bannister, J.J. Hollis, and R.J. Hurley, 2012: Anatomy of a catastrophic wildfire: The Black Saturday Kilmore East fire in Victoria, Australia, *Forest Ecology and Management*, **284**, 269 – 295, doi: 10.1016/j.foreco.2012.02.035.

4   Cruz M.G., Gould J.S., Alexander M.E., Sullivan A.L., McCaw W.L., Matthews S., 2015: *A Guide to Rate of Fire Spread Models for Australian Vegetation*. CSIRO Land and Water Flagship, Canberra, ACT, and AFAC, Melbourne, Vic, 123pp.

5   Ellis, P. F. M., 2013: Firebrand characteristics of the stringy bark of messmate (Eucalyptus obliqua) investigated using non-tethered samples. International Journal of Wildland Fire 2011, 22, 642‑651, doi: 10.1071/WF12141.

6   Engel, C. B., Lane, T. P., Reeder, M. J., and Rezney, M., 2012: The meteorology of Black Saturday. *Quarterly Journal of the Royal Meteorological Society*, **139**, 585–599.

7   Hall, J., P. F. Ellis, G. J. Cary, G. Bishop, and A. L. Sullivan, 2015: Long-distance spotting potential of bark strips of a ribbon gum (Eucalyptus viminalis). *International Journal of Wildland Fire*, **24**, 1109‑1117, doi: 10.1071/WF15031.

8   Hodgson, A., 1967: Fire management in eucalypt forest. In: *Proceedings of 6th Annual Tall Timbers Fire Ecology Conference*, March 6-7, 1967, Tallahassee, Florida. Chaired by E.V. Komarek, Tall Timbers Research Station, Tallahassee, Florida.

9   Kepert, J. D., and R. J. B. Fawcett, 2013: Meteorological Aspects of the Margaret River Fires of November 2011. *20th International Congress on Modelling and Simulation*, Adelaide, Australia, The Modelling and Simulation Society of Australia and New Zealand Inc., 180–186, doi: 10.36334/modsim.2013.A3.kepert.

10   Kepert J, Tory K, Ching E, Fawcett R, Schroeter S, Thurston W, Wilke D, and Zovko-Rajak D, 2022a: Improved predictions of severe weather to reduce community impact. Final project report, Bushfire and Natural Hazards CRC, Melbourne. 194 pp. Available from https://www.bnhcrc.com.au/sites/default/files/managed/downloads/improved_predictions_of_severe_weather_final_project_report.pdf.

11   Kepert, J. D., W. Thurston and K. J. Tory, 2022b: A fast, physically based model of ember transport by bushfire plumes. In preparation.

12   Kepert, J. D., 2022c: *Implementing Firebrand Transport in Spark 2.0*. Project progress report, 11 pp.

13   McArthur, A. G., 1966: *Weather and grassland fire behaviour*. Department of National Development, Forestry and Timber Bureau, Leaflet 100, 23 pp.

14   McArthur, A. G., 1967: *Fire behaviour in eucalypt forests*. Leaflet 107, Department of National Development Forestry and Timber Bureau, Canberra, 38 pp.

15   McArthur, A.G., 1969: The fire control problem and fire research in Australia. *Proceedings of the 1966 Sixth world forestry congress, vol. 2*. Spanish Minister of Agriculture, Madrid, pp. 1986–1991.

16   Peace, M., L. McCaw, B. Santos, J. D. Kepert, N. Burrows, and R. J. B. Fawcett, 2017: Meteorological drivers of extreme fire behaviour during the Waroona bushfire, Western Australia, January 2016. J. *S. Hem. Earth Sys. Sci.*, **67**, 79‑106, doi: 10.22499/3.6702.002.

17   Peace, M., J. Greenslade, H. Ye and J. D. Kepert, 2022: Simulations of the Waroona fire using the coupled atmosphere-fire model ACCESS-Fire. *J. South. Hem. Earth Systems Sci.*, doi: 10.1071/ES22013.

18   Peace M, Hanstrum B, Greenslade J, Zovko-Rajak D, Santra A, Kepert J, Fox-Hughes P, Ye H, Shermin T & Jones J: 2021: *Coupled fire-atmosphere simulations of five Black Summer fires using the ACCESS-Fire model - Black Summer*. Final report, Bushfire and Natural Hazards CRC, Melbourne. 74 pp. Available from https://www.naturalhazards.com.au/sites/default/files/2022-03/coupled_fire-atmosphere_simulations_black_summer_final_report.pdf.

19   Su, C.-H., Eizenberg, N., Steinle, P., Jakob, D., Fox-Hughes, P., White, C. J., Rennie, S., Franklin, C., Dharssi, I., and Zhu, H., 2019: BARRA v1.0: the Bureau of Meteorology Atmospheric high-resolution Regional Reanalysis for Australia, *Geosci. Model Dev.*, **12**, 2049-2068, doi: 10.5194/gmd-12-2049-2019.

20   Thomas, C. M., J. J. Sharples, and J. P. Evans, 2019: The terminal-velocity assumption in simulations of long-range ember transport. *Mathematics and Computers in Simulation*, **175**, 96–107, doi: 10.1016/j.matcom.2019.08.008.

21   Thurston, W., J. D. Kepert, K. J. Tory, and R. J. B. Fawcett, 2017: The contribution of turbulent plume dynamics to long-range spotting. *International Journal of Wildland Fire*, **26**, 317–330, doi: 10.1071/WF16142.

22   Toivanen, J., Engel, C. B., Reeder, M. J., Lane, T. P., Davies, L., Webster, S., et al., 2019: Coupled atmosphere-fire simulations of the Black Saturday Kilmore East wildfires with the Unified Model. *Journal of Advances in Modeling Earth Systems*, **11**, doi:10.1029/2017MS001245.

23   Weil, J. C., 1998: Plume rise. *Lectures on Air Pollution Modeling*, A. Venkatram, and J. C. Wyngaard, Eds., Amer. Meteor. Soc., 119‑166, doi: 10.1007/978-1-935704-16-4 4.

24   Wikipedia, 2022: *Eyre Peninsula bushfire, 2005*. Wikipedia. Available at: https://en.wikipedia.org/wiki/Eyre_Peninsula_bushfire,_2005. Accessed 7 November 2022.

25   Wilke, D. J., J. D. Kepert and K. J. Tory, 2022: The meteorology of the Tathra bushfire. *Weather and Forecasting*, **37**, 581 – 600, doi: 10.1175/WAF-D-21-0084.1.